Contents lists available at ScienceDirect

Bioactive Materials

Diatomite-incorporated hierarchical scaffolds for osteochondral regeneration

Cuijun Deng [a,d,1], Chen Qin [b,1], Zhenguang Li [a,1], Laiya Lu [c], Yifan Tong [a], Jiaqi Yuan [a], Feng Yin [c,**], Yu Cheng [a,***], Chengtie Wu [b,*]

[a] Shanghai Key Laboratory of Anesthesiology and Brain Functional Modulation, Clinical Research Center for Anesthesiology and Perioperative Medicine, Translational Research Institute of Brain and Brain-Like Intelligence, Shanghai Fourth People's Hospital, School of Medicine, Tongji University, Shanghai, 200434, PR China
[b] State Key Laboratory of High Performance Ceramics and Superfine Microstructure, Shanghai Institute of Ceramics, Chinese Academy of Sciences, Shanghai, 200050, PR China
[c] Department of Joint Surgery, Shanghai East Hospital, School of Medicine, Tongji University, 150 Jimo Road, Shanghai, 200032, PR China
[d] State Key Laboratory of Molecular Engineering of Polymers, Department of Macromolecular Science, Fudan University, Shanghai, 200438, PR China

ARTICLE INFO

ABSTRACT

Osteochondral regeneration involves the highly challenging and complex reconstruction of cartilage and subchondral bone. Silicon (Si) ions play a crucial role in bone development. Current research on Si ions mainly focuses on bone repair, by using silicate bioceramics with complex ion compositions. However, it is unclear whether the Si ions have important effect on cartilage regeneration. Developing a scaffold that solely releases Si ions to simultaneously promote subchondral bone repair and stimulate cartilage regeneration is critically important. Diatomite (DE) is a natural diatomaceous sediment that can stably release Si ions, known for its abundant availability, low cost, and environmental friendliness. Herein, a hierarchical osteochondral repair scaffold is uniquely designed by incorporating gradient DE into GelMA hydrogel. The adding DE microparticles provides a specific Si source for controlled Si ions release, which not only promotes osteogenic differentiation of rBMSCs (rabbit bone marrow mesenchymal stem cells) but also enhances proliferation and maturation of chondrocytes. Moreover, DE-incorporated hierarchical scaffolds significantly promoted the regeneration of cartilage and subchondral bone. The study suggests the significant role of Si ions in promoting cartilage regeneration and solidifies their foundational role in enhancing bone repair. Furthermore, it offers an economic and eco-friendly strategy for developing high value-added osteochondral regenerative bioscaffolds from low-value ocean natural materials.

1. Introduction

In recent years, multifunctional scaffolds have demonstrated significant potential in the regeneration of bone and cartilage tissues [1]. However, the integrated repair of cartilage and subchondral bone remains a substantial challenge due to their physiological anisotropy [2]. To achieve satisfactory regeneration of osteochondral defects, there is an urgent need for a dual-layer scaffold capable of providing the specific anisotropic physiological microenvironments for cartilage and subchondral bone formation, respectively. Recently, 3D printing technology, known for its high precision and rapid prototyping capabilities, has become increasingly popular in constructing multifunctional layered scaffolds [3–5]. This technology enables the precise fabrication of bioactive scaffolds tailored to meet various biochemical microenvironment requirements [6–8]. Owing to its multifunctionality, 3D printing has been utilized in the construction of numerous tissue engineering scaffolds with capabilities for mechanical or biochemical factor regulation, including artificial blood vessels, hearts, and bones [9–11].

Therefore, employing 3D printing technology to create hierarchical scaffolds presents a promising approach for regenerating osteochondral tissue [12].

To further enhance repair capabilities of 3D printing scaffolds, various inorganic biomaterials have been incorporated into hydrogels [13–15]. Owing to Si's role in promoting collagen and extracellular matrix synthesis and deposition during tissue repair, various Si-containing biomaterials have been used in tissue engineering for repair purposes [16,17]. However, these materials typically employed in research are predominantly complex silicate ceramics, making it challenging to conduct studies solely on the effects of pure Si ions on osteochondral tissue repair. Although Si dioxide releases only Si ions, traditional methods of fabricating micro/nanostructured silica dioxide (SiO_2) are complex and cumbersome, often introducing impurities that greatly limit its clinical application [18]. Most artificially synthesized silica dioxides are characterized by a densely crystalline structure, which results in a slow release of Si ions [19]. This property does not meet the rapid release requirements necessary for effective cartilage and bone tissue repair. Therefore, it is urgently necessary to find a natural biogenic silica that can rapidly and stably release Si ions continuously for cartilage and bone regeneration.

Encouragingly, we have discovered a natural diatom sedimentary mineral in the ocean that can stably release Si ions. Diatomite, composed of the siliceous skeletal remains of diatoms, possesses a uniform porous structure, high surface area, and excellent mechanical strength [20,21]. Owing to these advantages, diatomite has found widespread use in biomedical engineering, with applications including hemostasis, drug delivery, and skin repair [22–24]. More importantly, as a stable source of Si ions, diatomite can continuously release bioactive Si ions, promoting tissue repair. Therefore, it is reasonable to hypothesize that this economic and eco-friendly natural mineral material could be utilized to construct bioactive scaffolds for osteochondral repair, featuring stable Si ion release capability.

Herein, DE-incorporated hierarchical scaffolds for osteochondral regeneration were successfully fabricated using 3D printing technology (Scheme 1). Due to the excellent biocompatibility and significance in the field of cartilage repair of GelMA (gelatin methacryloyl), bioactive DE microparticles were selected and mixed with a GelMA solution to create a GelMA composite ink with gradient DE microparticles for 3D printing [25–28]. The incorporation of DE microparticles significantly improved the adhesion and proliferation of chondrocytes and rBMSCs. Furthermore, the DE-incorporated hierarchical scaffolds may promote the maturation of chondrocytes and induce osteogenic differentiation of rBMSCs through the ECM (Extracellular Matrix) receptor interaction signaling pathway. Additionally, in a New Zealand White rabbit osteochondral defect model, the introduction of DE microparticles was confirmed to substantially accelerate the regeneration of cartilage and subchondral bone, as well as promote the integration of newly formed tissue with the surrounding tissues. Overall, the economic and eco-friendly DE-incorporated hierarchical scaffolds are considered promising candidates for enhancing the regeneration of osteochondral tissue.

2. Results

2.1. Fabrication and characterization of DE-incorporated scaffolds

Prior to application, DE microparticles were filtered through a 30 μm membrane. The SEM (Scanning Electron Microscopy) image showed that the obtained DE microparticles had a rod-like shape with a length of
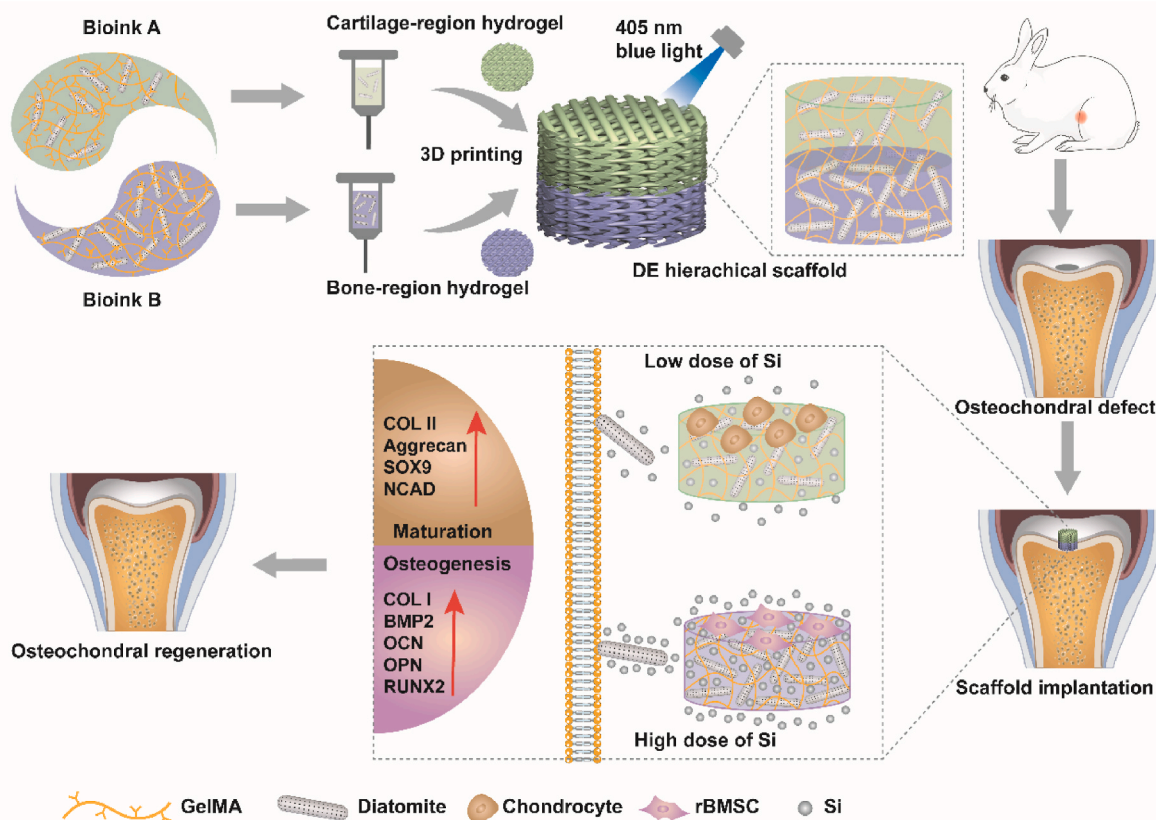
Scheme 1. Schematic illustration showing DE-incorporated hierarchical scaffold designed for osteochondral regeneration. The DE-incorporated hierarchical scaffold offers a conducive physiological microenvironment for the adhesion and proliferation of chondrocytes and rBMSCs. Moreover, the DE-incorporated hierarchical scaffold significantly stimulates the regeneration of hyaline cartilage and subchondral bone through the release of Si ions from the DE microparticles. Note: Bioink A and Bioink B are GelMA bioinks incorporated with different concentrations of DE microparticles.

less than 20 μm (Fig. 1A). It was also observed that these particles exhibited a well-organized and richly porous surface structure. Results from EDS (Energy-Dispersive X-ray Spectroscopy) analysis revealed that DE microparticles predominantly consist of silicon (Si) and oxygen (O) elements, with the Si to O ratio closely aligning with the composition of SiO_2 (Figs. S1A–E). Due to the carbon coating applied to the DE microparticles before conducting EDS analysis, carbon was also detected in the elemental composition results. In Fig. 1B, the XRD (X-ray Diffraction) pattern of the DE microparticles displayed distinct peaks at 22.0° and 26.6°, which could be indexed to SiO_2 in the form of quartz, as referenced in PDF No. 46–1045 (Fig. 1B). Moreover, results from ICP-AES (Inductively Coupled Plasma Atomic Emission Spectroscopy)

showed that DE microparticles could continuously and steadily release Si ions, with the ion release increasing as the concentrations of DE microparticles rose (Fig. S1F).

In the preparation of GelMA and DE-incorporated scaffolds, a 6 % (v/v) GelMA solution was combined with different concentrations of DE dispersion to form specialized printing inks suitable for GelMA, 5 % DE-incorporated GelMA (5 DE), 10 % DE-incorporated GelMA (10 DE), 20 % DE-incorporated GelMA (20 DE), and 30 % DE-incorporated GelMA (30 DE) scaffolds. Subsequently, the GelMA and DE-incorporated scaffolds were fabricated by 3D printing method. According to the XRD patterns, the distinct peaks observed at 22.0° and 26.6° were typical of quartz, indicating the presence of DE microparticles in the DE-incorporated
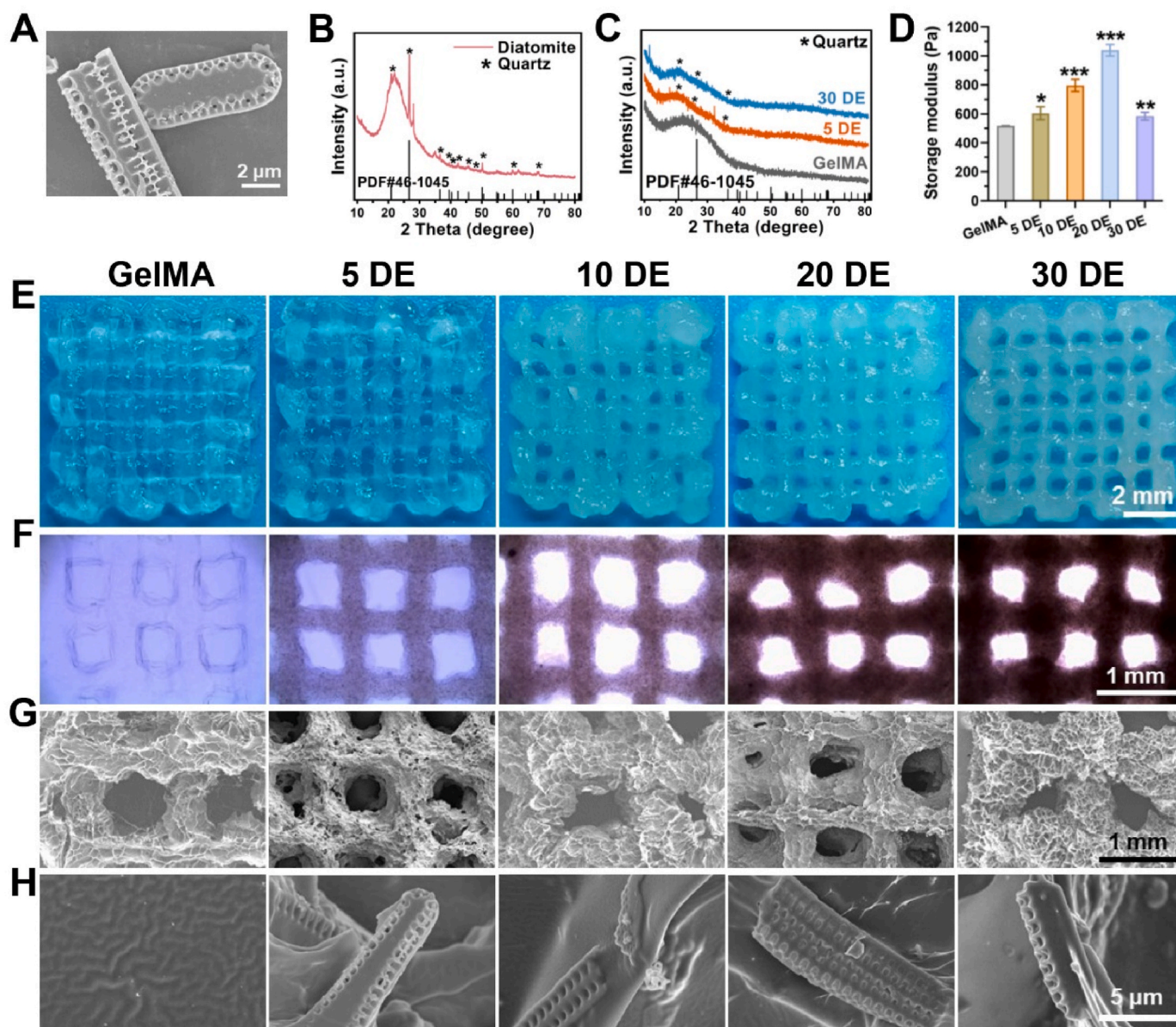
Fig. 1. Characterizations of DE microparticles and DE-incorporated scaffolds. (A) SEM image of DE microparticles, (B) XRD pattern of DE microparticles, (C) XRD patterns of GelMA scaffold and DE-incorporated scaffolds, (D) Maximum storage modulus of the scaffolds within 500 % strain, (E) Digital photographs of GelMA scaffold and DE-incorporated scaffolds, (F) Photographs of GelMA scaffold and DE-incorporated scaffolds taken under an inverted microscope, (G, H) SEM images of GelMA scaffold and DE-incorporated scaffolds. The XRD patterns confirmed the presence of the SiO_2 phase in DE microparticles and DE-incorporated scaffolds, characterized by the quartz structures, corresponding to PDF Nos. 46–1045. Furthermore, mechanical property testing revealed that the incorporation of DE microparticles significantly enhanced the storage modulus of the scaffolds. Additionally, SEM images showed that, in contrast to the smooth surface of the GelMA scaffold, the surface of the DE-incorporated scaffolds contained rod-shaped porous DE microparticles. Statistical comparisons were made between the GelMA scaffold and DE-incorporated scaffolds, with significance levels indicated as **p < 0.01 and ***p < 0.001, using one-way ANOVA followed by Dunnett's multiple comparisons test. The error bars in the results denote the mean ± standard deviation.

scaffolds (Fig. 1C). To investigate the impact of DE incorporation on the mechanical properties of hydrogels, detailed rheological and compression experiments were conducted on the DE-incorporated scaffolds. Results indicated that as the concentration of DE microparticles in the hydrogel increased, there was an initial rise followed by a decrease in the elastic modulus. The incorporation of DE significantly increased the storage modulus of hydrogel from 493.3 Pa (GelMA) to 1010.2 Pa (20 DE), elevated the Young's modulus from 64.2 kPa to 122.7 kPa, and raised the shear stress from 906 Pa to 1580 Pa (Fig. 1D and Figs. S2A–E). The compressive strength of the DE-incorporated scaffolds also improved as the DE concentration increased, with the 10 DE and 20 DE scaffolds achieving maximum compressive stresses of 16.85 kPa and 16.13 kPa, respectively (Fig. S2F). However, when the concentration of DE microparticles reached 30 %, the excess DE microparticles acted as

points of stress concentration, leading to a significant deterioration in mechanical properties. Moreover, results from ICP-AES indicated that scaffolds integrated with DE microparticles were capable of releasing Si ions in a continuous and stable manner. Notably, the rate of ion release escalated in conjunction with the increase in DE content (Fig. S2G). Visual inspection through optical photographs revealed that the 3D printed scaffolds featured a regular grid-like structure. It was also observed that the light transmittance of theses scaffolds diminished progressively with an upsurge in DE concentration (Fig. 1E, F). SEM images of the freeze-dried scaffolds showed that DE-incorporated scaffolds possessed an interconnected porous structure, with the surface covered in elongated DE microparticles featuring regular pores (Fig. 1G, H). Additionally, the enlarged SEM images displayed that the DE microparticles were homogeneously distributed within the hierarchical
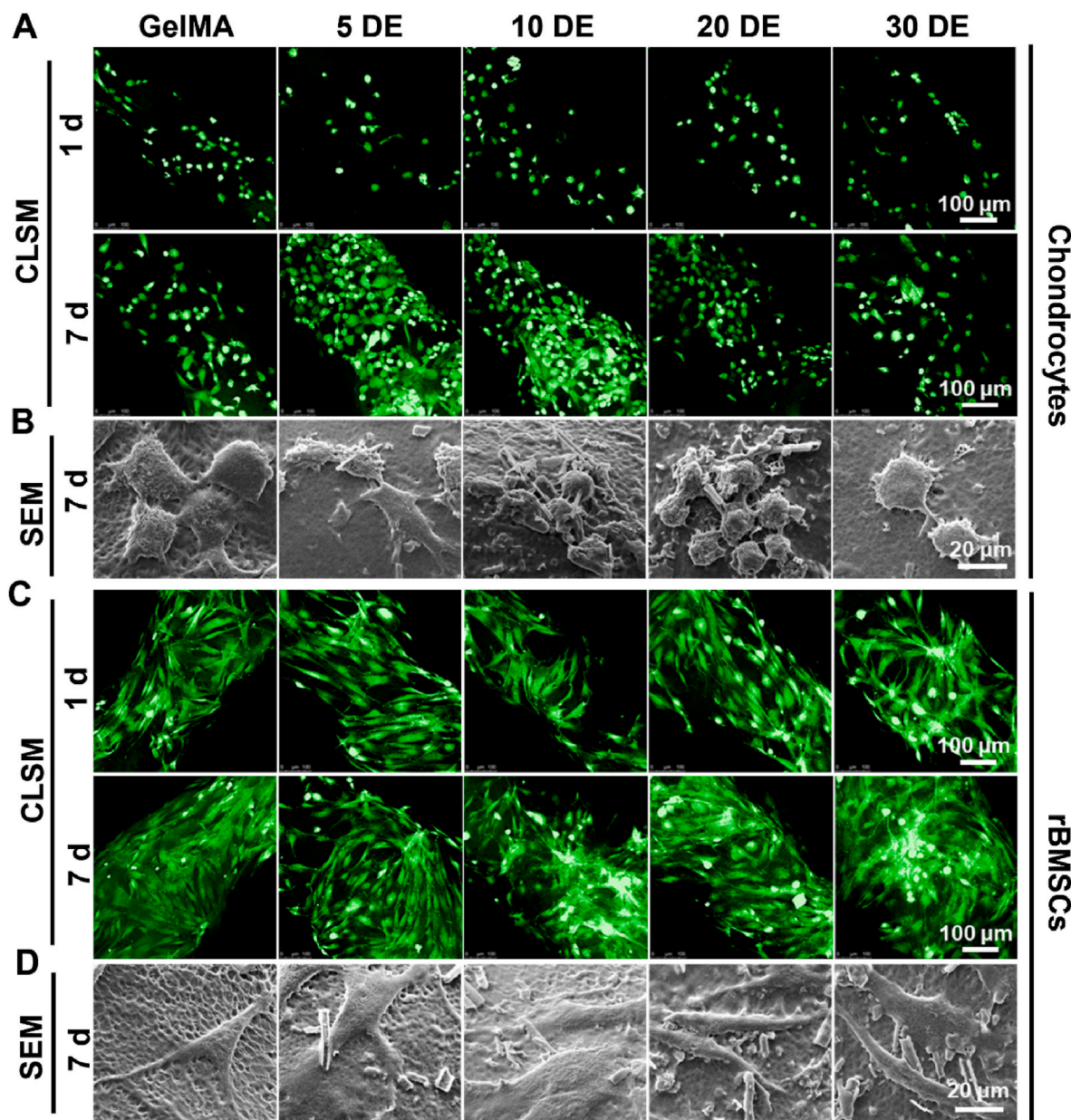
Fig. 2. Morphology of chondrocytes and rBMSCs cultured on GelMA scaffold and DE-incorporated scaffolds. (A) CLSM images of chondrocytes cultured on scaffolds for 1 and 7 days, (B) SEM images of chondrocytes cultured on scaffolds for 7 days, (C) CLSM images of rBMSCs cultured on scaffolds for 1 and 7 days, (D) SEM images of rBMSCs cultured on scaffolds for 7 days. The results demonstrated that chondrocytes proliferated and spread better on the 5 DE and 10 DE scaffolds compared to the GelMA scaffold. For rBMSCs, there was no significant difference in proliferation across different scaffolds. However, rBMSCs on the 20 DE and 30 DE scaffolds appeared more three-dimensional and fuller with abundant pseudopodia. The SEM images displayed that the chondrocytes and rBMSCs interacted with DE microparticles.

scaffold (Fig. S3). And the mapping images highlighted a uniform dispersion of DE microparticles across the surface of the scaffold. This dispersion was accompanied by a discernible enhancement in the presence of Si elements, which directly correlated with the increased DE concentration (Fig. S3). Concurrently, the release of Si ions resulting from the degradation of DE-incorporated scaffolds facilitated mineralization processes. Observations detailed in Fig. S4 illustrated that as the DE content increased, there was a corresponding increase in the mineral composition on the surface of scaffolds. The EDS analysis revealed that the calcium-to-phosphorus ratio of these surface minerals closely resembles that of hydroxyapatite (Figs. S4B–E). This similarity suggested an environment favorable for the regeneration of cartilage and bone.

2.2. DE-incorporated scaffolds promoted cell adhesion and differentiation

To further investigate the stimulating effects of DE-incorporated scaffolds on cell proliferation and adhesion, chondrocytes and rBMSCs were seeded onto the scaffolds, respectively. Subsequently, CLSM (Confocal Laser Scanning Microscopy) and SEM analyses were employed to observe cell proliferation and morphology. The results indicated that one day post-seeding, there were no significant differences in the proliferation of chondrocytes on different scaffolds (Fig. 2A). However, by day 7, chondrocytes on the 5 DE and 10 DE scaffolds were notably more abundant compared to other scaffolds, suggesting their superior ability to promote chondrocyte proliferation (Fig. 2A). Moreover, Cryo-SEM images revealed that chondrocytes with abundant pseudopodia on the surfaces of 5 DE scaffold had a greater contact area than those on the other scaffolds (Fig. 2B). Regardless of the culture duration, whether 1 day or 7 days, rBMSCs exhibited similar proliferation abilities on different scaffolds (Fig. 2C). However, those on the 20 DE and 30 DE scaffolds exhibited richer pseudopodia and a more three-dimensional morphology, indicating that the incorporation of DE promoted rBMSCs' attachment to the scaffolds (Fig. 2D). It was also observed that chondrocytes and rBMSCs interacted with the DE microparticles on the surfaces of the scaffolds, suggesting that DE microparticles may promote cell adhesion and proliferation.

On this basis, the impact of DE-incorporated scaffolds on the maturation of chondrocytes and the osteogenic differentiation of rBMSCs was
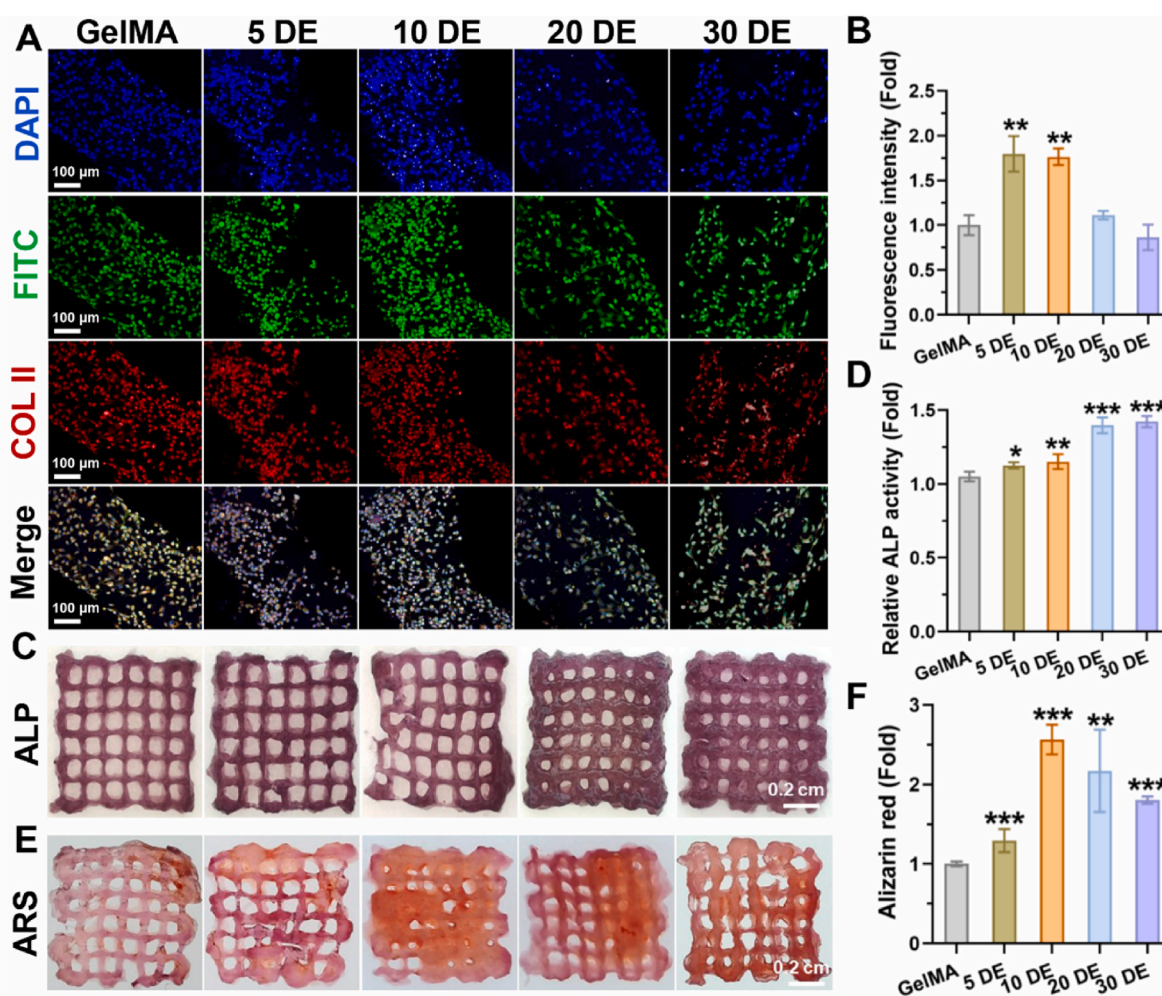
Fig. 3. DE-incorporated scaffolds promoted the maturation of chondrocytes and osteogenic differentiation of rBMSCs. (A) CLSM images of COL II expression after chondrocytes cultured on scaffolds for 3 days. (blue, DAPI for nucleus; green, FITC-phalloidin for cytoskeleton; red, Proteintech SA00013-4 secondary antibody for COL II), (B) Quantitative fluorescence intensity of COL II expression by using image-pro plus software, (C) ALP staining images after rBMSCs cultured on scaffolds for 14 days, (D) Quantitative ALP activity by PNPP method after rBMSCs cultured on scaffolds for 14 days, (E) Alizarin red staining images after rBMSCs cultured on scaffolds for 21 days, (F) Quantitative Alizarin red by CPC method after rBMSCs cultured on scaffolds for 21 days. As compared to the GelMA scaffold, chondrocytes cultured on the 5 DE and 10 DE scaffolds exhibited higher expression of COL II protein, suggesting the efficacy of 5 DE and 10 DE scaffolds in enhancing chondrocyte maturation. Furthermore, the qualitative and quantitative experimental results of ALP and ARS revealed that incorporating DE microparticles favors the osteogenic differentiation of rBMSCs. For comparison, the quantitative data of GelMA groups was normalized to a value of 1. Statistical comparisons were made between the GelMA groups and other groups, with significance levels indicated as $*p < 0.05$, $**p < 0.01$ and $***p < 0.001$, using one-way ANOVA followed by Dunnett's multiple comparisons test. The error bars in the results denote the mean ± standard deviation.

further explored. Immunofluorescence staining for COL II protein revealed that, compared to GelMA scaffolds, the 5 DE and 10 DE scaffolds significantly enhanced the expression of COL II in chondrocytes (Fig. 3A, **B**). However, the expression of COL II by chondrocytes on the 20 DE and 30 DE scaffolds was not significantly different from that on the GelMA scaffolds. Additionally, qualitative results from ALP staining and quantitative analysis showed that the incorporation of DE notably increased ALP activity, which progressively rose with higher DE content

and stabilized at a 20 % concentration (Fig. 3C, **D**). Alizarin red staining indicated that the DE-incorporated scaffolds significantly promoted the formation of calcium nodules, peaking at a DE concentration of 10 % (Fig. 3E, **F**). To further observe the morphology of osteogenically differentiated rBMSCs on the scaffolds, after 21 days of culture, the cellular samples were fixed and underwent Cryo-SEM analysis. It was found that the rBMSCs were in contact with the DE microparticles on the surface of the DE-incorporated scaffolds, and there were more calcified
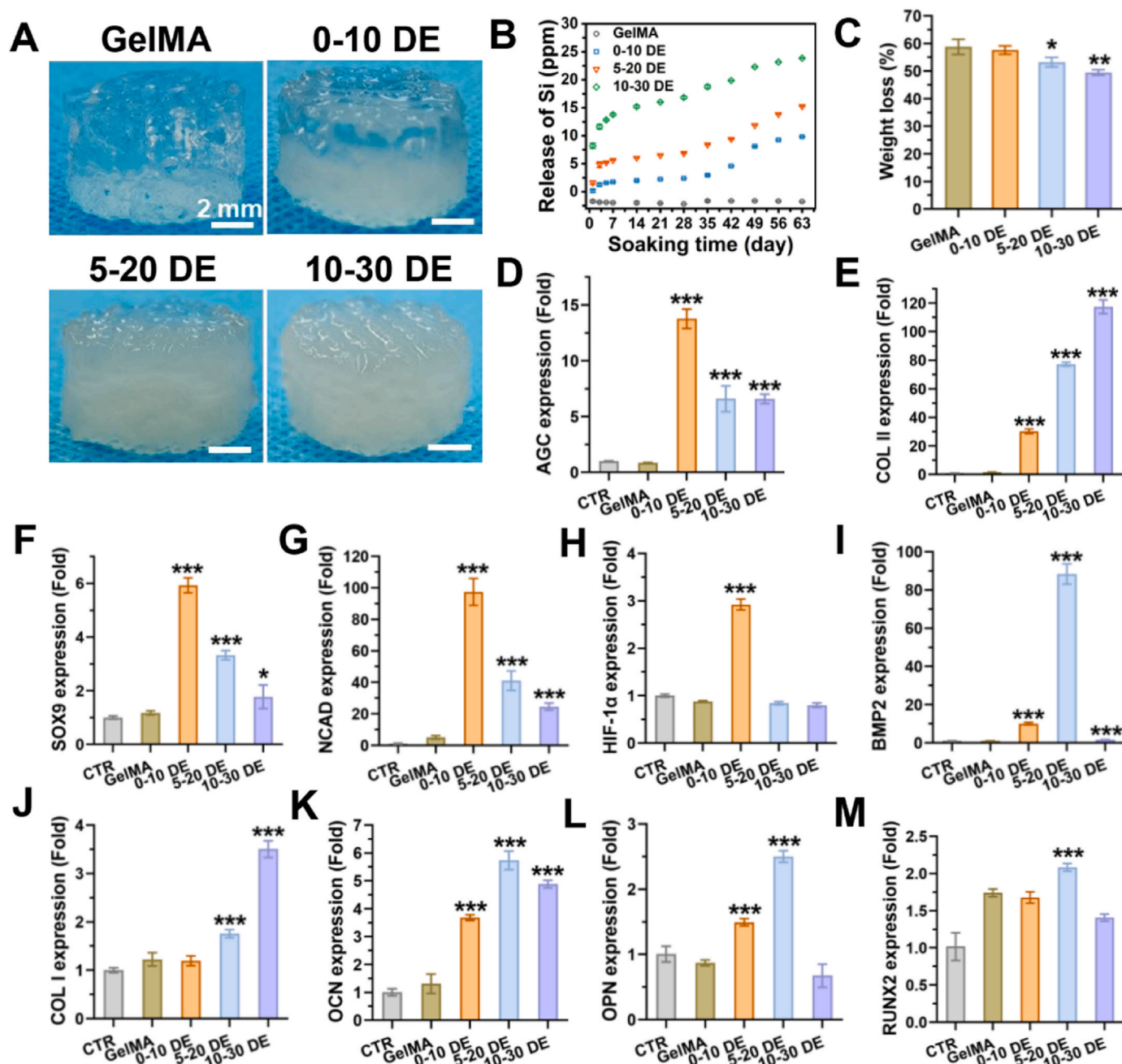
Fig. 4. Characterizations of DE-incorporated hierarchical scaffolds. (A) Digital photographs of DE-incorporated hierarchical scaffolds, (B) Release profiles of Si in DE-incorporated hierarchical scaffolds, (C) Weight loss of DE-incorporated hierarchical scaffolds after 63 days, (D–H) Expression of chondrogenic-related genes AGC, COL II, SOX9, NCAD, and HIF-1α after chondrocytes cultured on scaffolds for 7 days, (I–M) Expression of osteogenic-related genes BMP2, COL I, OCN, OPN, and RUNX2 after rBMSCs cultured on scaffolds for 7 days. It was found that Si can be continuously released from the DE-incorporated hierarchical scaffolds, and their degradation rates slow down as the DE content increases. Furthermore, 0–10 DE scaffold significantly enhanced the expression of genes related to chondrocyte maturation, while 5–20 DE scaffold significantly promoted the expression of genes associated with osteogenic differentiation in rBMSCs. For comparison, the gene expression in the CTR groups (without scaffold) was normalized to a value of 1. Statistical comparisons were made between the GelMA groups and other DE-incorporated hierarchical scaffolds groups, with significance levels indicated as *p < 0.05 **p < 0.01, and ***p < 0.001, using one-way ANOVA followed by Dunnett's multiple comparisons test. The error bars in the results denote the mean ± standard deviation.

secretions from the cells on the surface of the DE-incorporated scaffolds (Fig. S5). These results suggested that the incorporation of DE particles not only aided in promoting chondrocyte maturation but also enhancing osteogenic differentiation in rBMSCs.

2.3. Preparation and characterization of DE-incorporated hierarchical scaffolds

The aforementioned results indicated that GelMA, 5 DE, and 10 DE scaffolds were more suitable for cartilage repair, while the 10 DE, 20 DE, and 30 DE scaffolds exhibited superior performance in osteogenic induction. Therefore, GelMA, 5 DE, and 10 DE were selected as the upper layers of the scaffold, and 10 DE, 20 DE, and 30 DE served as the lower layers for fabricating a DE-incorporated hierarchical scaffold for osteochondral regeneration. Digital photographs illustrated that, due to varying DE concentrations in the upper and lower layers, hierarchical scaffolds exhibited different levels of transparency between the top and bottom halves (Fig. 4A). The transparency of the hierarchical scaffolds gradually decreased as the DE concentration increased. Results from ICP-AES showed that DE-incorporated hierarchical scaffolds could steadily and continuously release Si ions, with the ion release increasing as the DE content rose (Fig. 4B). The introduction of DE microparticles also enhanced the degradation properties of the scaffolds. Compared to GelMA scaffolds, the degradation of the 5–20 DE and 10–30 DE scaffolds was significantly slower, which is advantageous for the long-term requirements of cartilage and subchondral bone regeneration (Fig. 4C).

2.4. Stimulatory effect of DE-incorporated hierarchical scaffolds on chondrocytes and rBMSCs

Building on the study of physicochemical properties, the biological performance of the DE-incorporated hierarchical scaffolds was further investigated. Results from CCK8 assays indicated that DE-incorporated hierarchical scaffolds significantly promoted the proliferation of chondrocytes, while they had no promotional effects on the proliferation of rBMSCs (Fig. S6). Results from qPCR (quantitative Polymerase Chain Reaction) further revealed that the DE-incorporated hierarchical scaffolds significantly boosted the expression of genes specific to cartilage, including AGC, SOX9, COL II, NCAD, and HIF-1α (Fig. 4D–H). Among these, the 0–10 DE scaffold was the most effective in promoting chondrocyte maturation. Additionally, the DE-incorporated hierarchical scaffolds also notably elevated the expression of osteogenic differentiation-related genes in rBMSCs, such as BMP2, COL I, OCN, OPN, and RUNX2, with the 5–20 DE scaffold showing the most pronounced osteogenic induction effect (Fig. 4I-M). These results demonstrated that DE-incorporated hierarchical scaffolds possess excellent capabilities in promoting osteochondral regeneration.

2.5. Widespread transcriptomic alterations triggered by DE-incorporated hierarchical scaffolds

To explore the possible mechanism through which DE-incorporated scaffolds induce chondrocytes maturation and foster rBMSCs osteogenic differentiation, transcriptomic analyses were conducted on cells cultured on hierarchical scaffolds. Chondrocytes and rBMSCs grown on GelMA scaffolds (n = 3), 0–10 DE scaffolds (n = 3), and 5–20 DE scaffolds (n = 3) for 7 days were collected and underwent RNA-seq analysis. The levels of gene expression were standardized by determining the number of fragments per kilobase of transcript for every million mapped reads. Comparisons between the GelMA, 0–10 DE, and 5–20 DE groups were conducted to identify differentially expressed genes (DEGs) in the cellular samples following incubation with hierarchical scaffolds. The heatmap of all DEGs following cluster analysis revealed significant changes in chondrocyte transcriptome profiles among the different groups (Fig. S7A). Specifically, 826 upregulated and 626 downregulated DEGs were detected in the 0–10 DE group compared to the GelMA group

(Fig. S7B). In the comparison of 5–20 DE versus GelMA, 1324 genes were significantly upregulated, while the expression of 1193 genes were significantly downregulated (Fig. S7C). These results suggested that both 0–10 DE and 5–20 DE scaffolds triggered strong cellular responses in chondrocytes. The overlap of DEGs in paired comparisons showed that only 88 DEGs were identical, while 139 DEGs changed in the 0–10 DE versus GelMA comparison, and 1159 DEGs changed in the 5–20 DE versus GelMA comparison, demonstrating the strong effects of the 0–10 DE and 5–20 DE scaffolds on chondrocytes (Fig. S7D). To further elucidate the promotive effects of hierarchical scaffolds on chondrocyte activity, a Gene Ontology (GO) enrichment analysis was executed to delineate the biological functions implicated by these DEGs. Fig. 5A and B display the top GO terms for biological processes (BP), cellular components (CC), and molecular functions (MF) based on the p-value, revealing the notable effects of DE-incorporated hierarchical scaffolds on chondrocytes. Several key GO terms were significantly enriched in BP, such as "extracellular structure organization", "extracellular matrix organization", "regulation of cell mobility", "positive regulation of cell mobility", "regulation of cell adhesion", "cell adhesion", "positive regulation of biomineralization", "positive regulation of developmental process", "regulation of cartilage development", and "cartilage development" (Fig. 5A, B). These results suggested that DE-incorporated hierarchical scaffolds could regulate multifaceted functions involved in cartilage repair, including cell migration and adhesion, ECM deposition, and cartilage formation. Afterward, we used Kyoto Encyclopedia of Genes and Genomes (KEGG) enrichment analysis to uncover the major signaling pathways that changed in chondrocytes grown on scaffolds with DE incorporated into their hierarchical structure. Results indicated that several signaling pathways of chondrocytes were potentially changed after stimulation by DE-incorporated hierarchical scaffolds, including ECM-receptor interaction, TNF signaling pathway, and IL-17 signaling pathway (Fig. 5C, D). Moreover, transcript profiles showed that multiple genes of the ECM-receptor interaction pathway in chondrocytes were significantly increased, including ITGB6, COL4A6, LAMA3, ITGA8, ITGA3, ITGA4, IBSP, ITGAV, and ITGB8 (Fig. 5E).

Additionally, transcriptomic analyses were also conducted on rBMSCs cultured on hierarchical scaffolds. The heatmap of all DEGs following cluster analysis uncovered significant changes in rBMSC transcriptome profiles among the groups of GelMA, 0–10 DE, and 5–20 DE (Fig. S8A). Briefly, 149 upregulated and 81 downregulated DEGs were detected in the 0–10 DE group compared to the GelMA group (Fig. S8B). In the comparison of 5–20 DE versus GelMA, the expression of 408 genes was significantly upregulated, while the expression of 370 genes was significantly downregulated (Fig. S8C). The overlap of DEGs in paired comparisons showed that only 17 DEGs were identical, while 100 DEGs changed in the 0–10 DE versus GelMA comparison, and 512 DEGs changed in the 5–20 DE versus GelMA comparison, indicating the significant effects of 0–10 DE and 5–20 DE scaffolds on rBMSCs (Fig. S8D). To further study the positive effect of hierarchical scaffolds on rBMSCs, GO enrichment analysis was conducted. Fig. 6A and B display the top GO terms for CC, MF, and BP based on the p-value, revealing the obvious effects of DE-incorporated hierarchical scaffolds on rBMSCs. Several key GO terms were significantly enriched in BP, such as "glycosaminoglycan binding", "positive regulation of cytosolic calcium ion concentration", "cell adhesion", "positive regulation of cell migration", "positive regulation of cell mobility", "biological adhesion", and "multicellular organismal response to stress", (Fig. 6A, B). Furthermore, results from KEGG enrichment revealed that several signaling pathways were potentially changed under the stimulation of DE-incorporated hierarchical scaffolds, including ECM-receptor interaction, PPAR signaling pathway, and synaptic vesicle cycle signaling pathway (Fig. 6C, D). In the transcriptional profiles of rBMSCs using RNA-seq, the 0–10 DE and 5–20 DE groups displayed significantly higher expression of relevant genes in the ECM-receptor interaction pathway, such as HMMR, ITGA2, ITGB4, IBSP, and CD36, compared to the GelMA group, which was subsequently validated by qPCR (Fig. 6E).
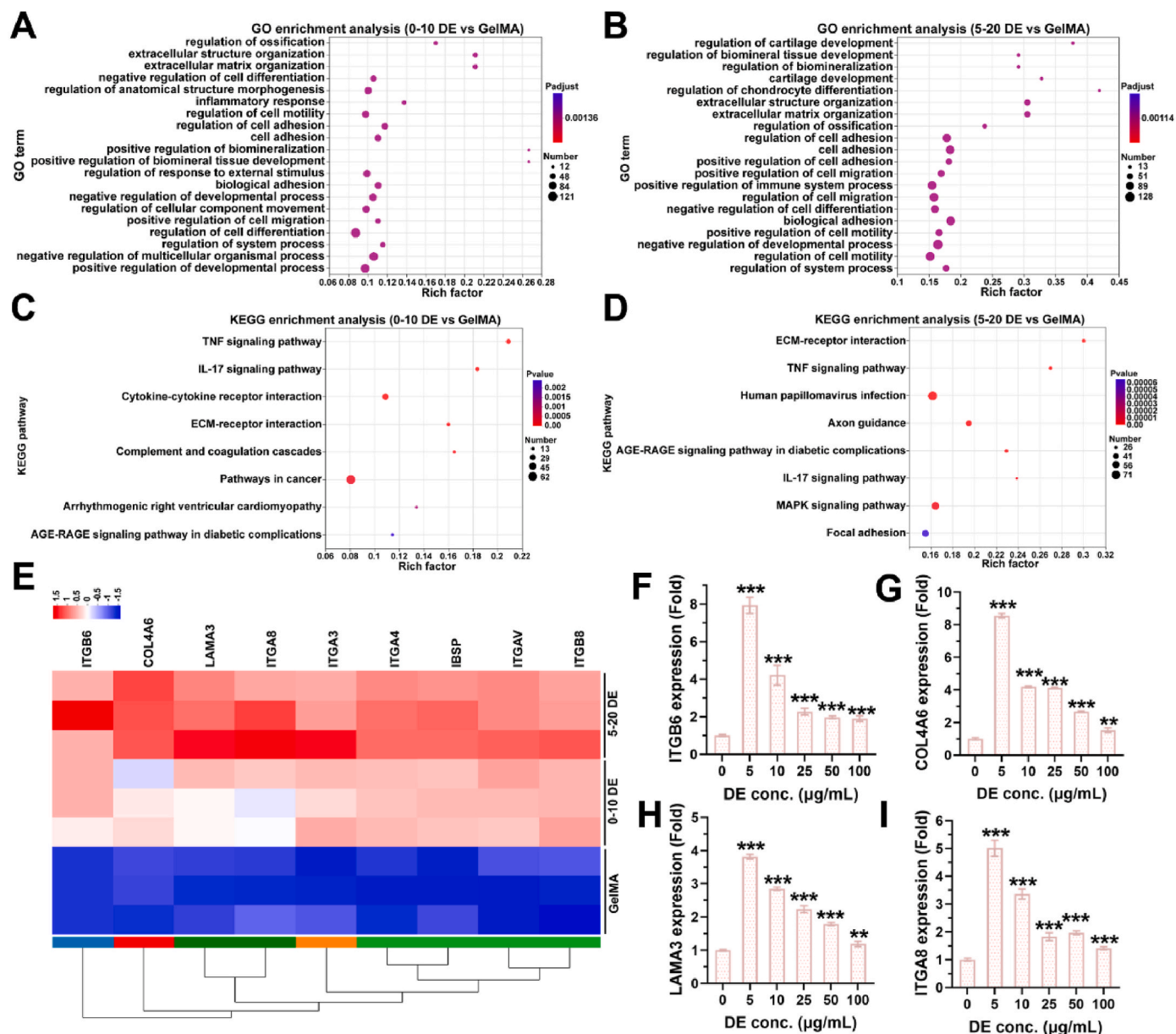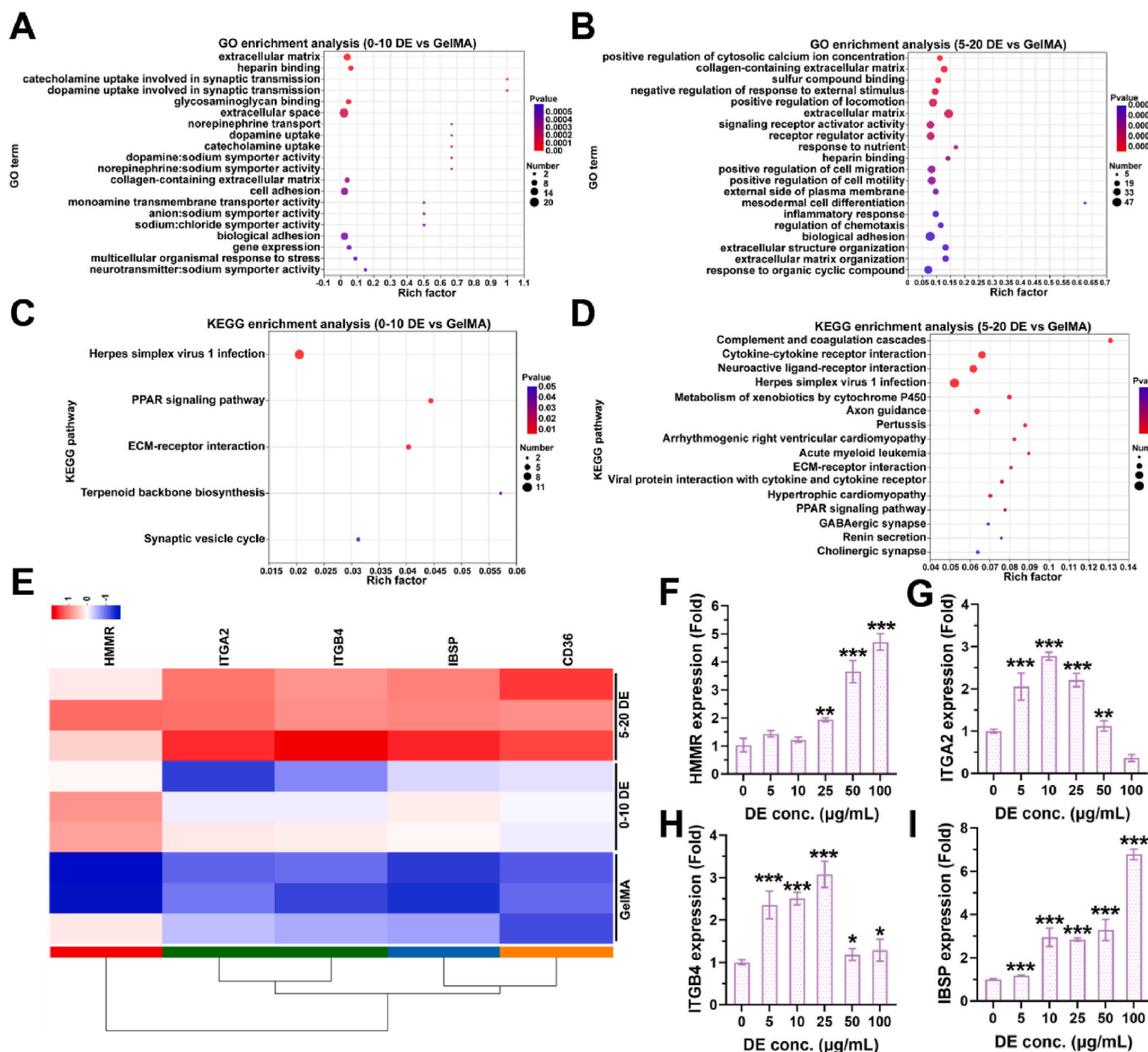
Fig. 5. RNA-seq reveals widespread transcriptomic changes of chondrocytes triggered by DE-incorporated hierarchical scaffolds. (A) Significant GO terms associated with ECM organization and cell adhesion (0–10 DE versus GelMA), (B) Significant GO terms associated with cartilage development and ECM organization (5–20 DE versus GelMA), (C) Top 8 KEGG enrichment pathways in the comparison of 0–10 DE versus GelMA, (D) Top 8 KEGG enrichment pathways in the comparison of 5–20 DE versus GelMA, (E) Heatmap of expression levels in ECM-receptor interaction pathway related genes using RNA-seq, (F–I) mRNA levels of ECM-receptor interaction pathway related genes after chondrocytes co-cultured with different concentrations of DE microparticles for 7 days. For comparison, the gene expression in the CTR groups (0 μg/mL) was normalized to a value of 1. Statistical comparisons were made between the CTR groups and other groups, with significance levels indicated as **p < 0.01 and ***p < 0.001, using one-way ANOVA followed by Dunnett's multiple comparisons test. The error bars in the results denote the mean ± standard deviation.

2.6. DE microparticles promoted chondrocytes maturation and rBMSCs differentiation

To further investigate the stimulatory effect of DE microparticles on osteochondral regeneration, different concentrations of DE microparticles were used to incubate chondrocytes and rBMSCs. Results from the CCK8 assay showed that low concentrations of DE microparticles (5–50 μg/mL for chondrocytes and 5–10 μg/mL for rBMSCs) had no significant impact on their proliferation, whereas concentrations above 50 μg/mL demonstrated a suppressive effect on proliferation (Fig. S9A, C). Crystal violet staining further confirmed these results. Additionally, PCR results indicated that low concentrations (5–10 μg/mL) of DE microparticles significantly promoted the expression of chondrocyte-specific genes,

such as COL II, Aggrecan, SOX9, NCAD, and HIF-1α (Fig. S10). Immunofluorescence staining results further confirmed that low concentrations of DE microparticles could enhance the production of COL II protein in chondrocytes (Fig. S11A). The quantitative analysis revealed that as the concentration of DE microparticles increased, their stimulatory effect on COL II protein expression gradually decreased (Fig. S11B). Apart from promoting chondrocyte maturation, DE microparticles also significantly enhanced osteogenic differentiation in rBMSCs. Results from mRNA detection showed that within the concentration range of 10–100 μg/mL, DE microparticles significantly stimulated the activation of genes associated with osteogenesis (BMP2, COL I, OCN, OPN, and RUNX2) in rBMSCs (Fig. S12). Qualitative and quantitative analyses of the early osteogenic marker ALP and the late marker calcium nodules of

Fig. 6. RNA-seq reveals widespread transcriptomic changes of rBMSCs triggered by DE-incorporated hierarchical scaffolds. (A) Significant GO terms associated with ECM (0–10 DE versus GelMA), (B) Significant GO terms associated with positive regulation of cytosolic calcium ion and collagen-containing ECM (5–20 DE versus GelMA), (C, D) Several top KEGG enrichment pathways in the comparison of 0–10 DE versus GelMA and 5–20 DE versus GelMA, (E) Heatmap of expression levels in ECM-receptor interaction pathway related genes using RNA-seq, (F–I) mRNA levels of ECM-receptor interaction pathway related genes after rBMSCs co-cultured with different concentrations of DE microparticles for 7 days. For comparison, the gene expression in the CTR groups (0 μg/mL) was normalized to a value of 1. Statistical comparisons were made between the CTR groups and other groups, with significance levels indicated as *p < 0.05, **p < 0.01 and ***p < 0.001, using one-way ANOVA followed by Dunnett's multiple comparisons test. The error bars in the results denote the mean ± standard deviation.

osteogenic differentiation indicated that DE microparticles obviously upregulated the expression of ALP and calcium nodules (Fig. S13). To further explore the mechanism by which DE microparticles regulate chondrocyte maturation and rBMSC osteogenic differentiation, relevant genes in the ECM signaling pathway were examined. It was found that multiple genes of the ECM-receptor interaction pathway in chondrocytes were significantly increased, including ITGB6, COL4A6, LAMA3, ITGA8, ITGA3, ITGA4, IBSP, ITGAV, and ITGB8 (Fig. 5F–I, Fig. S14). The relevant genes of the ECM-receptor interaction pathway in rBMSCs were subsequently validated by qPCR (Fig. 6F–I, Fig. S15).

2.7. DE-incorporated hierarchical scaffolds promoted the in vivo osteochondral regeneration

Although the 10–30 DE scaffold exhibited the highest levels of COL I and COL II expression, it's important to note that the pathways leading to chondrogenesis or osteogenesis are influenced by a broader spectrum of genes beyond COL II and COL I. Key genes such as Aggrecan, SOX9, NCAD, HIF-1α, BMP2, OCN, OPN, and RUNX2 also play crucial roles in these differentiation processes. Considering the collective expression profiles of these essential genes, the 10–30 DE scaffold does not represent the most favorable option for *in vivo* study. Based on their excellent *in vitro* chondrogenesis and osteogenesis, the 0–10 DE and 5–20 DE scaffolds were selected for subsequent *in vivo* studies of osteochondral

repair. A model of osteochondral defects was created in New Zealand White rabbits via surgical methods, with the hierarchical scaffolds being inserted into the areas of defect. Optical images revealed that the newly formed cartilage in the 0–10 DE and 5–20 DE groups was continuous and smooth, in contrast to the fragmentary cartilage observed in the CTR and GelMA groups (Fig. 7A–C). To determine whether the new tissue was fibrous or bony, Micro-CT analysis was further conducted. Transverse and sagittal views of the Micro-CT analysis showed that large voids with relatively less new bone formation remained unhealed in the defects of the CTR and GelMA groups, while the 0–10 DE and 5–20 DE groups exhibited significant neo-bone formation (Fig. 7B). At 12 weeks, the neo-bone tissue in the 5–20 DE group was abundant and well-distributed in the defect region, whereas residual void spaces were found in the other groups (Fig. 7D). To further investigate the quality of the new bone, quantitative analyses of BMD (bone mineral density), BV/TV (relative bone volume fraction), and Tb. N (trabecular number) were conducted on the knee samples. Statistical analysis revealed a significant increase in BMD within the 5–20 DE group compared to other groups (Fig. 7E). The BV/TV and Tb. N in the 0–10 DE and 5–20 DE groups were markedly elevated compared to the CTR and GelMA groups at the 12-week mark (Fig. 7F and G). These parameters gradually increased over time, indicating that the quality of the new bone improved as the healing process progressed.

Building on the promising results of the Micro-CT analysis, histological analysis was subsequently performed to further evaluate the regenerative potential of hyaline cartilage and subchondral bone *in vivo*. In Figs. 8 and 9, the area between the red arrows indicates the location of the osteochondral defect creation. The outcomes of H&E staining indicated an absence of inflammatory responses across all experimental groups, and new tissue was observed in the defect regions (Fig. 8). However, the cartilage and bone tissue regeneration in the CTR group was relatively weak. In the GelMA group, a mixture of fibrous and bone

tissues partially filled the defect regions, and gaps still existed at 12 weeks, indicating incomplete repair. In the 0–10 DE and 5–20 DE groups, abundant neo-tissue was found in the defect regions at 8 weeks. By the 12th week, the surface of the newly formed tissue was continuous and integrated well with the surrounding native tissue. Furthermore, DE-incorporated hierarchical scaffolds exhibited superior degradation properties to GelMA scaffolds. Upon closer examination in the enlarged images, increased amounts of new tissue and DE microparticles were observed in the 0–10 DE and 5–20 DE scaffolds.

To further investigate the regenerative potential of hyaline cartilage and subchondral bone *in vivo*, SO (Safranin O/Fast Green) staining and Masson's trichrome (MA) staining were conducted. Results of SO staining revealed that the 0–10 DE and 5–20 DE groups exhibited a substantial presence of cartilage-like translucent tissue at 8 and 12 weeks (Fig. 9A, **B**). In contrast, the CTR and GelMA groups had defects that were partially filled with a mixture of cartilage-like and fibrous tissues. The tidemark is a distinct histological structure that acts as a barrier to prevent the calcification of the transparent cartilage and stop blood vessels from penetrating through the calcified cartilage layer into the transparent cartilage. In the 0–10 DE and 5–20 DE groups, at both 8 and 12 weeks, the calcified cartilage layer structure was relatively intact, with a clear demarcation between cartilage and subchondral bone. In contrast, the CTR and GelMA groups did not exhibit a distinct calcified cartilage layer, and partial tissue defects remained unrepaired in the subchondral bone area. MA staining of osteochondral sections further substantiated the aforementioned observations, revealing an abundant presence of collagen fibers with the newly formed tissue (Fig. 9C, **D**). To further identify the types of collagen fibers in the new tissues, immunofluorescence staining of collagen fibers was performed. The results revealed that integration of DE microparticles notably enhanced the expression of COL II protein in the neo-cartilage tissue and elevated the expression of COL I protein in newly formed bone tissue
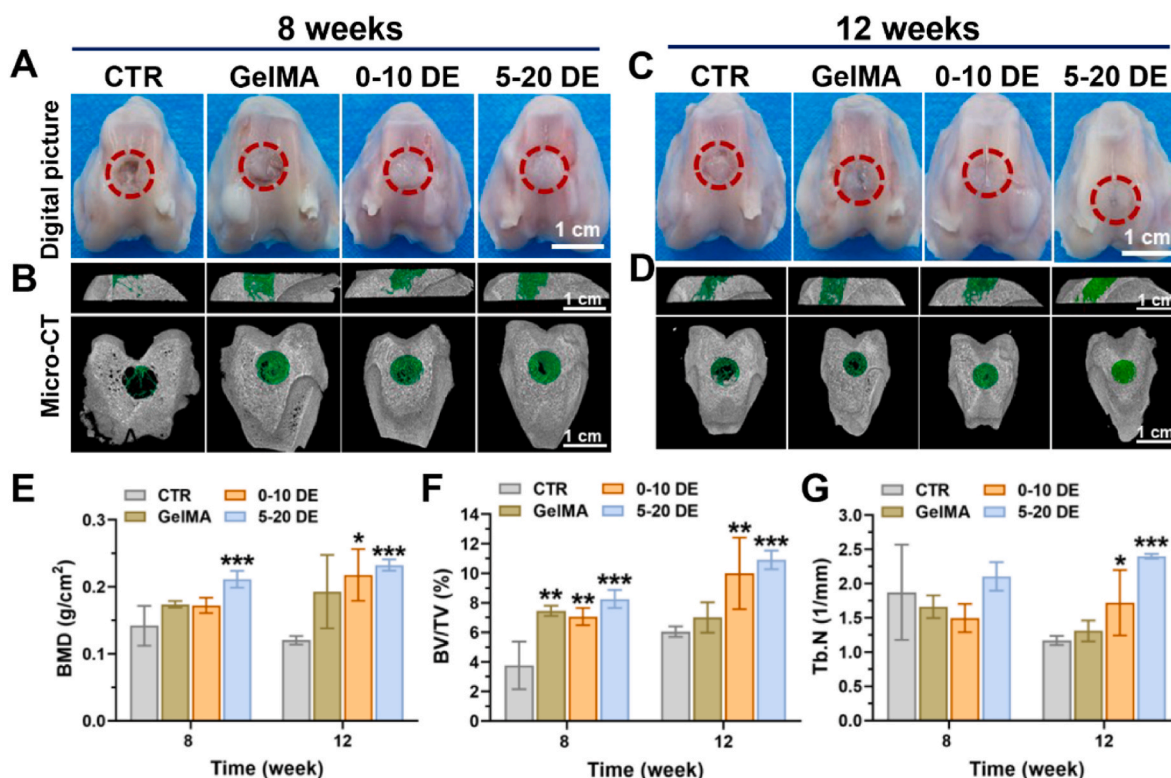
Fig. 7. Digital photographs and Micro-CT analysis of knee samples post-surgery. (A) Digital photograph of knee samples at 8 weeks, (B) Micro-CT images of the knee samples at 8 weeks, (C) Digital photograph of knee samples at 12 weeks, (B) Micro-CT images of the knee samples at 12 weeks, (E–G) Quantitative analysis of BMD, BV/TV, and Tb.N. Statistical comparisons were made between the CTR groups and other groups, with significance levels indicated as *$p < 0.05$, **$p < 0.01$ and ***$p < 0.01$, using one-way ANOVA followed by Dunnett's multiple comparisons test. The error bars in the results denote the mean ± standard deviation.
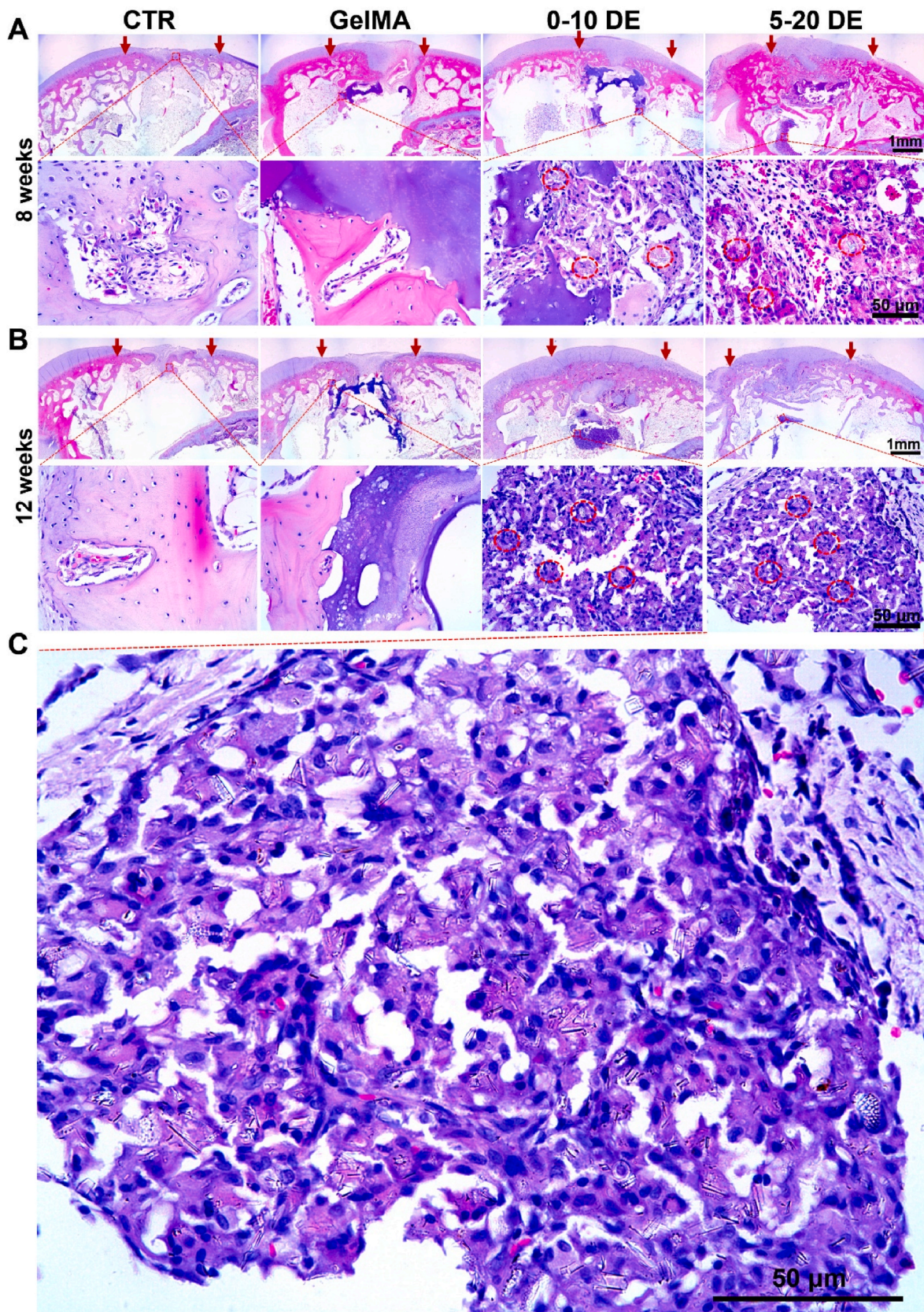
Fig. 8. H&E staining of osteochondral sections. (A) 8 weeks, (B) 12 weeks, (C) The enlarged image of H&E staining in 5–20 DE group at 12 weeks. The enlarged images showed that the DE-incorporated hierarchical scaffolds exhibited superior degradation properties, with a notable presence of DE microparticles within the neo-tissue. Partial DE microparticles were marked in the red circles. The area between the red arrows indicates the location of the osteochondral defect creation.
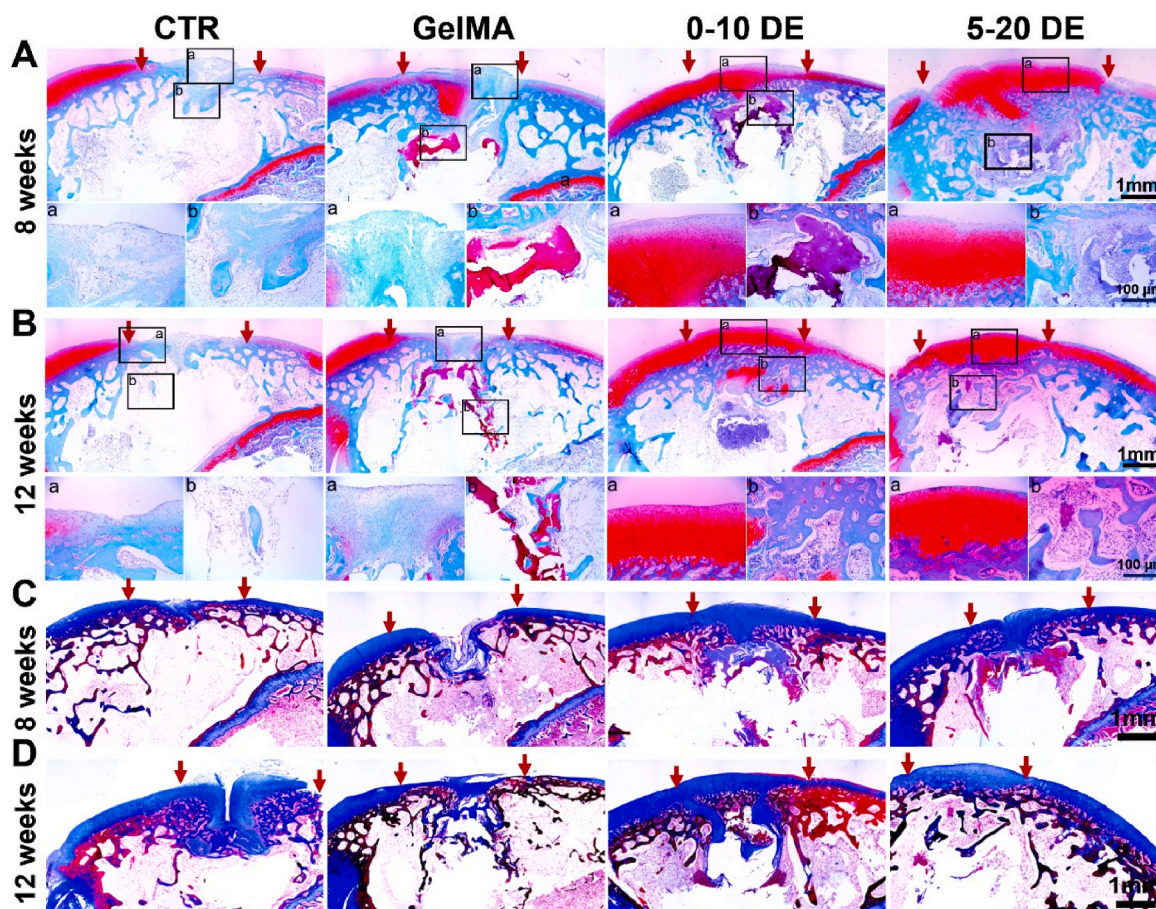
Fig. 9. Osteochondral regeneration *in vivo*. (A, B) Safranin O-fast green staining, (C, D) MA staining. Results from Safranin O-fast green staining and MA staining demonstrated that the DE-incorporated hierarchical scaffolds significantly promoted the regeneration of cartilage and subchondral bone. The area between the red arrows indicates the location of the osteochondral defect creation.

(Fig. S16, Fig. S17). The above results suggested a successful regeneration of hyaline cartilage and subchondral bone. Drawing on these results, the International Cartilage Repair Society (ICRS) scoring was applied, revealing that, in comparison to the CTR and GelMA groups, the 5–20 DE groups had higher scores at both 8 and 12 weeks (Fig. S18). Through histological and immunofluorescence analyses, it was demonstrated that scaffolds incorporating DE microparticles facilitated a significant enhancement in the regeneration of hyaline cartilage and subchondral bone tissue.

3. Discussion

Osteochondral regeneration is a complex and meticulously orchestrated physiological process, involving the reconstruction of both cartilage and subchondral bone. Due to the physiological anisotropy of them, it is a great challenge to integrated repair of cartilage and subchondral bone. Many efforts have been devoted to develop biomaterials for cartilage and bone regeneration [29–31], especially bioactive ions stimulation in artificial bioscaffolds [32–35]. Si ions play a crucial role in promoting collagen synthesis and secretion, acting as a crucial element in the bone development process. However, the majority of current research is focused on the promotion of bone repair by Si ions released from artificially synthesized materials, with limited studies on the effects of Si ions in promoting cartilage repair. Furthermore, most artificially synthesized biomaterials are high-cost and not eco-friendly, as well as often introducing impurities that greatly limit its clinical application. Therefore, utilizing low-cost natural and eco-friendly biomaterials to construct osteochondral regeneration scaffolds with

specially Si ions release is expected to solve the above problems.

Herein, a DE-incorporated hierarchical scaffold was successfully developed using 3D printing technology. On the one hand, the incorporation of DE microparticles significantly improved the mechanical properties of the hydrogel, making it more conducive to the adhesion and proliferation of chondrocytes and rBMSCs. The extent and strength of cell adhesion are significantly influenced by the matrix's elasticity [36–39]. Chondrocytes and rBMSCs struggle to adhere to surfaces with low stiffness, show limited cell interactions on surfaces of intermediate stiffness, and display enhanced spreading and numerous pseudopodia on surfaces with high stiffness [40–42]. In this study, the storage modulus, Young's modulus, and compressive strength of the scaffold increased with the DE microparticle content, peaking at a 20 % DE concentration. However, when the DE content reached 30 %, the excess DE became stress concentration points, leading to a significant decrease in mechanical properties [43]. CLSM and Cryo-SEM results indicated that, compared to GelMA scaffolds, chondrocytes exhibited better adhesion on the 5 DE and 10 DE scaffolds, which had higher mechanical properties. However, when the content of DE microparticles exceeded 10 %, cell adhesion decreased may due to the excess Si ions released from the scaffolds, surpassing the needs of the chondrocytes. For rBMSCs, the higher modulus provided by DE-incorporated scaffolds significantly promoted cell spreading and pseudopodia formation compared to GelMA scaffolds. To summarize, the incorporation of DE microparticles markedly improved the attachment and expansion of chondrocytes and rBMSCs on scaffolds that included DE.

The introduced DE microparticles not only improved the mechanical properties of the scaffolds but also released therapeutic ions, creating a

mechanical and biochemical microenvironment conducive to the regeneration of cartilage and subchondral bone. Numerous studies have shown that Si ions serve a vital function in the skeletal system, promoting the growth and development of both cartilage and bone [44,45]. Si actively facilitates the synthesis and secretion of the extracellular matrix in chondrocytes [46,47]. Previous research has indicated that Si can enhance the proliferation and osteogenic differentiation of rBMSCs and increase collagen synthesis [48,49]. In this study, the DE-incorporated hierarchical scaffolds were capable of stably and continuously releasing Si ions. The released Si ions effectively promoted COL II synthesis in chondrocytes and efficiently induced osteogenic differentiation of rBMSCs. Results from RNA sequencing further revealed that the transcriptome profiles of rBMSCs and chondrocytes cultured on the DE-incorporated hierarchical scaffolds were enriched in the ECM-receptor interaction signaling pathway. This pathway is closely involved in the proliferation and differentiation of both rBMSCs and chondrocytes [50,51]. Regulating the ECM can effectively promote chondrocyte adhesion and proliferation, as well as steer stem cells towards osteogenic differentiation [52,53]. Therefore, it is reasonable to propose that the DE-incorporated hierarchical scaffolds may promote chondrocyte maturation and induce osteogenic differentiation of rBMSCs by regulating the ECM-receptor interaction signaling pathway. To verify this hypothesis, we further cultured chondrocytes and rBMSCs with different concentrations of DE microparticles and assessed genes related to the ECM-receptor interaction pathway. Results indicated that DE microparticles significantly upregulated the expression of genes relevant to the ECM-receptor interaction pathway, including ITGB6, COL4A6, LAMA3, ITGA8, ITGA3, ITGA4, IBSP, ITGAV, ITGB8, HMMR, ITGA2, ITGB4, and CD36. Hence, the introduction of DE microparticles not only improved the mechanical properties of the hydrogel but also activated cellular biological behavior.

Additionally, results of the *in vivo* study demonstrated that DE-incorporated hierarchical scaffolds could effectively repair osteochondral tissue. Compared to the CTR and GelMA groups, the 0–10 DE and 5–20 DE groups exhibited more hyaline cartilage and subchondral bone in the defect region. On one hand, the DE-incorporated hierarchical scaffolds provided appropriate mechanical stimulation conducive to cell adhesion and proliferation. On the other hand, the silicon ions released from DE microparticles promoted the synthesis and mineralization of the extracellular matrix, accelerating the regeneration of cartilage and subchondral bone. Results from SO staining showed that in the 0–10 DE and 5–20 DE groups, the newly formed cartilage tissues were highly integrated with the surrounding tissues, with the tidemark and calcified cartilage layer structures being well-defined and distinct between the cartilage layer and the subchondral bone layer. Furthermore, results from immunofluorescence analyses revealed that integration of DE microparticles notably enhanced the expression of COL II protein in the neo-cartilage tissue and elevated the expression of COL I protein in newly formed bone tissue. Therefore, our results indicated that DE-incorporated hierarchical scaffolds, which provided stable Si ions release, could effectively promote osteochondral regeneration and restore its physiological function. To the best of our knowledge, this is the first osteochondral regeneration scaffold to achieve high value-added therapy using a low-value ocean natural material.

4. Conclusion

In this study, a DE-incorporated hierarchical scaffold with stable Si ion release functions was successfully prepared to provide specific anisotropic physiological microenvironments for cartilage and subchondral bone regeneration. DE-incorporated hierarchical scaffolds offered a suitable physiological microenvironment for the adhesion and proliferation of chondrocytes and rBMSCs. Importantly, these scaffolds may significantly stimulate the regeneration of hyaline cartilage and subchondral bone via the ECM-receptor interaction signaling pathway. The above results indicate that the DE-incorporated hierarchical

scaffolds, with stable Si ion release capability, can meet the needs for simultaneous cartilage and subchondral bone reconstruction, thus providing an economic and eco-friendly strategy for developing high value-added osteochondral regenerative bioscaffolds from low-value ocean natural materials.

5. Experiment section

Purification and characterization of DE microparticles: The DE microparticles were acquired from Sigma-Aldrich Co. Ltd. (USA) was purified by a 30 μm of filter membrane to obtain rod-shaped microparticles. The morphologies and element composition of DE microparticles were analyzed using a scanning electron microscope (SEM, SU8220, Hitachi, Japan) which equipped with energy-dispersive X-ray spectroscopy (EDS). The phase composition of DE microparticles was determined using X-ray diffraction analysis (Rigaku D/Max-2550 V, Geiger-Flex, Japan). To further investigate the Si ion release performance of DE microparticles, inductively coupled plasma atomic emission spectroscopy (ICP-AES, 710 ES, Varian, USA) was employed. The DE microparticles underwent treatment with cell culture medium (BL308A, Biosharp Life Sciences) over a series of time points: 1, 3, 5, 7, 14, 21, and 28 days. The concentrations of DE microparticles tested were 0, 5, 10, 25, 50 and 100 μg/mL.

Preparation of DE-incorporated scaffolds: In our preliminary experiments, we conducted a series of trials to determine the optimal concentration of GelMA. Ultimately, to achieve a balance between printability and shape fidelity, we selected a bioink containing 6 % GelMA for printing in subsequent experiments. Firstly, the sterilization of purified DE microparticles was achieved by exposing them to ultraviolet (UV) light for 2 h, after which they were mixed into sterile phosphate-buffered saline (PBS) to create varying concentrations of DE dispersions. Afterward, a 12 % (v/v) GelMA solution was added to the equivalent volume of DE dispersions, and thoroughly mixed to form the 3D printing inks containing 6 % of GelMA and gradient concentrations of DE microparticles (0 %, 5 %, 10 %, 20 % and 30 % DE microparticles). The above inks were firstly stored in 4 °C to form pre-gel. Subsequently, the pre-gel was expelled through a 27 G needle at 10 °C under proper air pressure to obtain primary scaffolds using a 3D printing device (GeSiM 3.2 Bioscaffolder, Germany). The initial scaffolds were subsequently subjected to blue light (405 nm) for approximately 45 s to induce the formation of cross-linked networks. The crosslinking agent used in this experiment was lithium phenyl-2,4,6-trimethylbenzoylphosphinate (LAP). The scaffolds printed with 0 %, 5 %, 10 %, 20 %, and 30 % of DE dispersions were named GelMA, 5 DE, 10 DE, 20 DE and 30 DE, respectively. The hierarchical scaffolds with different concentrations of DE microparticles at upper and lower layers were name GelMA (upper layer: GelMA, lower layer: GelMA), 0–10 DE (upper layer: GelMA, lower layer: 10 DE), 5–20 DE (upper layer: 5 DE, lower layer: 20 DE), and 10–30 DE (upper layer: 10 DE, lower layer: 30 DE).

Characterization of DE-incorporated scaffolds: The structure and morphology of DE-incorporated scaffolds was detected by using EVOS FL Auto imaging system (Life technologies, Thermo Fisher scientific, USA) and scanning electron microscopy (SEM, SU8220, Hitachi, Japan). The phase identification of scaffolds was conducted with an X-ray diffractometer (Rigaku D/Max-2550 V, Geiger-Flex, Japan) at a speed of 1°/min (10–80°). Before SEM and XRD analyses, the scaffolds were freeze-dried overnight. Furthermore, a Mars60 rotational rheometer equipped with a 20 mm parallel plate (Haake, Germany) was used to measure the viscoelasticity of DE-incorporated scaffolds. Strain sweeps (1–500 %) under 1 Hz were used to measure the shear yielding properties. All tests were conducted at room temperature. Furthermore, the Si release of DE-incorporated scaffolds was investigated. DE-incorporated scaffolds were treated with cell culture medium (BL308A, Biosharp Life Sciences) for 1, 3, 5, 7, 14, 21, and 28 days. The medium volume to scaffold mass was 0.1 g/mL. At the predetermined time, the medium was collected, and silicon levels were determined

through an inductively coupled plasma atomic emission spectroscopy (ICP-AES, 710 ES, Varian, USA). Following the ion release experiment, DE-incorporated scaffolds were freeze-dried, and the morphology and composition were characterized with a Hitachi SU8220 scanning electron microscopy.

Additionally, the degradation properties and Si release of DE-incorporated hierarchical scaffolds were also investigated. DE-incorporated hierarchical scaffolds treated with cell culture medium (BL308A, Biosharp Life Sciences) for 1, 3, 5, 7, 14, 21, 28, 35, 42, 49, 56, and 63 days. The medium volume to scaffold mass was 0.1 g/mL. At the predetermined time, the medium was collected, and silicon levels were determined through an inductively coupled plasma atomic emission spectroscopy (ICP-AES, 710 ES, Varian, USA). Following a 63-day incubation in cell culture medium, the scaffolds were dried for 24 h, after which their degradation rate was precisely quantified using a precision scale.

Cell culture of chondrocytes and rBMSCs: Chondrocytes were initially harvested from New Zealand White rabbits, followed by the culture of these isolated cells in Dulbecco's Modified Eagle Medium (DMEM, BL308A, Biosharp Life Sciences) enriched with 10 % fetal calf serum (FBS, FBSAD-01011-500, Cyagen Biosciences, China) and 1 % penicillin-streptomycin (PS, 15140122, Gibco, Thermo Fisher Scientific). Rabbit BMSCs (rBMSC, RABXMX-01001, Cyagen Biosciences, China) were provided by Cyagen Biosciences. And a matching bone marrow mesenchymal stem cell basal medium (RBXMX-9001, Cyagen Biosciences, USA) which contained 10 % FBS and 1 % PS was used to culture rBMSCs.

Cell proliferation assay: The growth of chondrocytes and rBMSCs incubated with different concentrations of DE microparticles was detected with a cell counting kit-8 (CK04, Dojindo, Japan). In Brief, cells were seeded into a 96-well plate (2×10^3 cells/well) and incubated with complete cell culture medium which contained different concentrations of DE microparticles. At the set time point, CCK-8 working solution was applied to incubate cells for 2 h, and the corresponding absorbance of the working solution was measured at 450 nm by using a multifunction microplate reader (ELx808, BioTek, USA). For a more vivid illustration of cell proliferation, cells were stained using a crystal violet assay (C0121, Beyotime Biotechnology Co. Ltd., China), and images were obtained with an EVOS FL Auto imaging system.

Proliferation and cell morphology of chondrocytes and rBMSCs on scaffolds: Chondrocytes (1.0×10^4 cells/well) and rBMSCs (1.0×10^4 cells/well) were seeded on the GelMA and DE-incorporated scaffolds in a 48-well plate, and the whole scaffolds were soaked with cell suspension. At specified time intervals, the scaffolds were relocated to a new 48-well plate, and a solution of CCK-8 reagent (CK04, Dojindo, Japan) was used to incubate with cells for 2 h. Subsequently, the CCK-8 working solution was transferred to a 96-well plate for absorbance measure. Before confocal laser scanning microscope (CLSM, TCS SP8, Leica, Germany) and Cryo-SEM (FEI Quanta 450, Frequency Electronics Inc., USA) analyses were conducted, chondrocytes and rBMSCs were anchored by 2.5 % glutaraldehyde. For CLSM observing, fluorescein-phalloidin (40735 ES, Yeasen, Shanghai, China) and diamidinophenylindole (DAPI, Sigma-Aldrich, USA) were used to stain cytoskeletons and nuclei.

Differentiation of chondrocytes and rBMSCs: Considering the enhanced cell adhesion and proliferation observed on the scaffolds, the specific genes of chondrocyte maturation and rBMSCs osteogenic differentiation were detected by RT-qPCR (quantitative real-time transcriptase polymerase chain reaction). After incubating with different concentrations (0, 5, 10, 25, 50 and 100 μg/mL) of DE microparticles for 7 days, the total RNAs of chondrocytes and rBMSCs were collected and reversely transcribed by applying a RNAprep Micro Kit (FSK 201, ToYoBo, Japan). And then, a $2 \times$ SG Fast qPCR Master Mix (B639272-0005, BBI Life Sciences, Shanghai, China) and a Step One Plus Real-Time PCR system (QuantStudio7, Thermofisher, USA) were used to conduct RT-qPCR. Following this, target gene expression was calculated and normalized using the $2^{-\Delta\Delta Ct}$ method. Furthermore, the promotion of DE-incorporated scaffolds on chondrocyte maturation and rBMSCs

osteogenic differentiation was also investigated. Chondrocytes (5.0×10^5 cells/well) and rBMSCs (5.0×10^5 cells/well) were seeded on the GelMA and DE-incorporated scaffolds in a 6-well plate, and the whole scaffolds were soaked with cell suspension. Subsequently, the scaffolds with cells were transferred to a new culture plate for following cultivation. After 7 days of incubation, total RNA was extracted for RT-qPCR. In chondrocytes, the target genes were Aggrecan (AGC), COL II, N-Cadherin (NCAD), SOX9 and HIF-1α. In rBMSCs, the target genes were COL I, BMP2, OCN, OPN, and RUNX2. Meanwhile, GAPDH was employed as the housekeeping gene in RT-qPCR analysis. The primer sequences were purchased from Bosun Biotechnology Co., Ltd (Shanghai, China), and the primer sequences were shown in Table S1.

Furthermore, the expression of COL II, which is a typical protein in chondrocyte, was detected by immunofluorescence technique. After exposing chondrocytes to varying concentrations of DE microparticles for 3 days, all chondrocytes were fixed using 2.5 % glutaraldehyde. Subsequently, a primary antibody (Proteintech, Cat No: 28459-1-AP, China) and second antibody (Proteintech, Cat No: SA00013-4, China) were used to incubate with the cellular samples. After that, fluorescein-phalloidin and DAPI were used to stain cytoskeletons and nuclei. To investigate the COL II expressed in the chondrocytes cultured on DE-incorporated scaffolds, same approach was used. Briefly, chondrocytes (5.0×10^4 cells/well) were seeded on the GelMA and DE-incorporated scaffolds in a 48-well plate. After 3 days of co-culturing, cellular samples were anchored by 2.5 % glutaraldehyde, following by the incubation of primary antibody and second antibody, as well as fluorescein-phalloidin and DAPI. Ultimately, argon laser lines at wavelengths of 405 nm, 488 nm, and 614 nm were employed to acquire CLSM images, and quantitative analysis was performed using Image-Pro Plus software.

In addition, ALP expression and calcium nodule formation of rBMSCs were further studied. After co-incubating with various concentrations of DE microparticles or DE-incorporated scaffolds in osteogenic induction medium for 14 days, the BCIP/NBT phosphatase color development kit (C3206, Beyotime, China) and an ALP assay kit (P0321, Beyotime, China) were applied to identify and quantify the expression of ALP in rBMSCs. The positive images of ALP and absorbance data were obtained from an EVOS FL Auto imaging system and a multifunction microplate reader (ELx808, BioTek, USA), respectively. To study the calcium nodules formation of rBMSCs incubated with different concentrations of DE microparticles or seeded on DE-incorporated scaffolds, ARS staining was conducted. Briefly, 1 % aqueous solutions of gelatin were used to incubate the 6-well plate for 30 min. Following this, rBMSCs were seeded in a 6-well plate and cultured in osteogenic induction medium containing varying concentrations of DE microparticles for a duration of 21 days. For ARS detection of DE-incorporated scaffolds, rBMSCs (5.0×10^5 cells/well) were seeded on the surfaces of scaffolds directly and incubated in osteogenic induction medium for 21 days. At the set time point, 2.5 % glutaraldehyde was used to fix cellular samples. Subsequently, ARS working solution (C0140, Beyotime Biotechnology Co. Ltd., China) was applied to stain the calcium nodules, and an EVOS FL Auto imaging system was applied to capture the images. To quantify the formation of calcium nodules, 100 mM cetylpyridinium chloride (Macklin, China) was used to incubate the cellular samples for 30 min and the absorbance data was detected at 570 nm with an ELx808 multifunction microplate reader. The preparation of the osteogenic induction medium with different concentrations of DE microparticles involved dispersing 1 mg of dried DE microparticles in the medium to create a final volume of 10 mL, resulting in a concentration of 100 μg/mL. And then, the obtained solution was diluted to 1/2 (50 μg/mL), 1/4 (25 μg/mL), 1/10 (10 μg/mL), and 1/20 (5 μg/mL). The rBMSCs incubated only with osteogenic induction medium were served as a control group (CTR).

RNA-sequencing and data analysis: To further study the underlying mechanisms of DE-incorporated hierarchical scaffolds inducing chondrocyte maturation and rBMSCs osteogenic differentiation, RNA-sequencing was conducted. Chondrocytes (5.0×10^5 cells/well) and

rBMSCs (5.0×10^5 cells/well) were seeded on the GelMA and DE-incorporated hierarchical scaffolds in a 6-well plate. After a seven-day incubation period, total RNA was extracted by using the TAKARA Trizol reagent. This was followed by the enrichment and fragmentation of mRNA, accomplished using Oligo DT beads and fragmentation buffer, respectively. Subsequently, cDNA was synthesized using the ToYoBo FSK 201 reverse transcription kit (ToYoBo, Japan). This cDNA was then converted to double-stranded DNA using the NEBNext mRNA Second Strand Synthesis Kit (E6111L, NEB, USA). Following the purification of the double-stranded cDNA, a PE library was constructed, and sequencing was performed on the Illumina Novaseq 6000 platform. In this study, the identification and analysis of differentially expressed genes were conducted using the DESeq2, while the generation of heatmaps was achieved through the pheatmap package. In the cellular samples, a gene was considered to be expressed if its count value was 1.0 or higher. For GO analysis, the DAVID and REVIGO tools were utilized. The evaluation of differentially expressed genes was conducted by using the DESeq2 package within the R programming environment. In this part of the study, three replicates were gathered, sequenced, and subsequently analyzed. A p-value of 0.05 or lower was deemed to signify statistical significance.

To further validate the results of the RNA-Seq sequencing, chondrocytes and rBMSCs were cultured with different concentrations of DE microparticles, and the expression of relevant genes were measured via RT-qPCR. The target genes for chondrocytes included ITGB6, COL4A6, LAMA3, ITGA8, ITGA3, ITGA4, IBSP, ITGAV, and ITGB8, while HMMR, ITGA2, ITGB4, IBSP and CD36 were the target genes for rBMSCs. Furthermore, GAPDH was used as the internal control gene in RT-qPCR analyses. The primer sequences for these analyses were obtained from Bosun Biotechnology Co., Ltd. (Shanghai, China), and are detailed in Table S1.

In vivo osteochondral regeneration: All procedures involving rabbits adhered to the stringent guidelines set forth by the Institutional Animal Care and Use Committee at Tongji University. To create an osteochondral defect model, twenty-four adult rabbits, each weighing approximately 2.5 kg, were utilized, with each defect measuring 6 mm in diameter and 6 mm in height. Following this, the GelMA and DE-incorporated hierarchical scaffolds were meticulously inserted into the defective region, with careful alignment of their top surfaces with the uppermost layer of the cartilage. The untreated defects were assigned to the blank control group (CTR, n = 6). Meanwhile, the remaining defects were treated differently: six received GelMA scaffolds, another six were implanted with 0–10 DE scaffolds, and the final six were embedded with 5–20 DE-incorporated hierarchical scaffolds. Knee samples were harvested at the 8-week and 12-week marks for the assessment of cartilage and subchondral bone regeneration. These samples were fixed in paraformaldehyde for 48 h before being analyzed using a Skyscan 1172 micro-CT scanner (Bruker, Germany) to acquire detailed bone information. The analysis of this data was conducted using Data Viewer and CTAn software. Moreover, CT vox software was utilized to generate transverse and sagittal views of the images. To assess the efficacy of osteochondral regeneration, staining techniques such as Hematoxylin and Eosin (H&E), Safranin O/Fast green (SO) and Masson′ trichrome (MA) were utilized. Moreover, immunofluorescence staining for COL II and COL I proteins was further performed to identify the types of collagen fibers in the new tissues. Optical images and immunofluorescence images of these sections were taken using an EVOS FL Auto imaging system. Furthermore, six evaluators, who were unaware of the study details, assigned ICRS scores for the analysis.

Statistical analysis: In this study, Graphpad prism software was employed for all statistical analysis, and the results was presented as means ± standard deviations. Detailed statistical parameters for each experiment are articulated in the legends accompanying the respective figures. Here, 'n' denotes the number of experimental replicates, while 'P' signifies the probability value. Furthermore, details regarding sample sizes and probability values can be found in the figure legends.

Statistically significant outcomes are indicated by a P value less than 0.05. The data were demonstrated with * for $0.01 < p < 0.05$, ** for $0.001 < p < 0.01$, and *** for $p < 0.001$.

Ethics approval and consent to participate

CRediT authorship contribution statement

Cuijun Deng: Writing – review & editing, Writing – original draft, Methodology, Investigation, Formal analysis, Data curation, Conceptualization. **Chen Qin:** Writing – review & editing, Writing – original draft, Investigation, Data curation, Conceptualization. **Zhenguang Li:** Writing – review & editing, Writing – original draft, Formal analysis. **Laiya Lu:** Writing – review & editing, Methodology. **Yifan Tong:** Writing – review & editing, Methodology. **Jiaqi Yuan:** Writing – review & editing, Methodology. **Feng Yin:** Writing – review & editing, Resources. **Yu Cheng:** Writing – review & editing, Resources, Funding acquisition, Conceptualization. **Chengtie Wu:** Writing – review & editing, Resources, Funding acquisition, Conceptualization.

Declaration of compering interest

Chengtie Wu serves on the editorial board of *Bioactive Materials* but did not participate in the editorial review process or in making the publication decision for this article. The authors have disclosed that there are no conflicts of interest.

Acknowledgements

Appendix A. Supplementary data

Supplementary data to this article can be found online at https://doi.org/10.1016/j.bioactmat.2024.05.004.

References

[1] R. Chen, J.S. Pye, J. Li, C.B. Little, J.J. Li, Multiphasic scaffolds for the repair of osteochondral defects: outcomes of preclinical studies, Bioact. Mater. 27 (2023) 505–545.

[2] C. Ai, Y.H.D. Lee, X.H. Tan, S.H.S. Tan, J.H.P. Hui, J.C.-H. Goh, Osteochondral tissue engineering: perspectives for clinical application and preclinical development, J. Orthop. Transl. 30 (2021) 93–102.

[3] F. Li, S.-F. Liu, W. Liu, Z.-W. Hou, J. Jiang, Z. Fu, S. Wang, Y. Si, S. Lu, H. Zhou, D. Liu, X. Tian, H. Qiu, Y. Yang, Z. Li, X. Li, L. Lin, H.-B. Sun, H. Zhang, J. Li, 3D printing of inorganic nanomaterials by photochemically bonding colloidal nanocrystals, Science 381 (6665) (2023) 1468–1474.

[4] M. Zeng, Y. Du, Q. Jiang, N. Kempf, C. Wei, M.V. Bimrose, A.N.M. Tanvir, H. Xu, J. Chen, D.J. Kirsch, J. Martin, B.C. Wyatt, T. Hayashi, M. Saeidi-Javash, H. Sakaue, B. Anasori, L. Jin, M.D. McMurtrey, Y. Zhang, High-throughput printing of combinatorial materials from aerosols, Nature 617 (7960) (2023) 292–298.

[5] J. Bauer, C. Crook, T. Baldacchini, A sinterless, low-temperature route to 3D print nanoscale optical-grade glass, Science 380 (6648) (2023) 960–966.

[6] M. Xie, Y. Shi, C. Zhang, M. Ge, J. Zhang, Z. Chen, J. Fu, Z. Xie, Y. He, In situ 3D bioprinting with bioconcrete bioink, Nat. Commun. 13 (1) (2022) 3597.

[7] S. Duraivel, D. Laurent, D.A. Rajon, G.M. Scheutz, A.M. Shetty, B.S. Sumerlin, S. A. Banks, F.J. Bova, T.E. Angelini, A silicone-based support material eliminates interfacial instabilities in 3D silicone printing, Science 379 (6638) (2023) 1248–1252.

[8] S. Gantenbein, E. Colucci, J. Kaech, E. Trachsel, F.B. Coulter, P.A. Ruehs, K. Masania, A.R. Studart, Three-dimensional printing of mycelium hydrogels into living complex materials, Nat. Mater. 22 (1) (2023) 128–134.

[9] W. Xiao, W. Chen, Y. Wang, C. Zhang, X. Zhang, S. Zhang, W. Wu, Recombinant DTβ4-inspired porous 3D vascular graft enhanced antithrombogenicity and recruited circulating CD93+/CD34+ cells for endothelialization, Sci. Adv. 8 (28) (2022) eabn1958.

[10] A. Lee, A.R. Hudson, D.J. Shiwarski, J.W. Tashman, T.J. Hinton, S. Yerneni, J. M. Bliley, P.G. Campbell, A.W. Feinberg, 3D bioprinting of collagen to rebuild components of the human heart, Science 365 (6452) (2019) 482–487.

[11] S. Camarero-Espinosa, L. Moroni, Janus 3D printed dynamic scaffolds for nanovibration-driven bone regeneration, Nat. Commun. 12 (1) (2021) 1031.

[12] J.M. Bliley, D.J. Shiwarski, A.W. Feinberg, 3D-bioprinted human tissue and the path toward clinical translation, Sci. Transl. Med. 14 (666) (2022) eabo7047.

[13] G.L. Koons, M. Diba, A.G. Mikos, Materials design for bone-tissue engineering, Nat. Rev. Mater. 5 (8) (2020) 584–603.

[14] H. Zhang, C. Qin, M. Zhang, Y. Han, J. Ma, J. Wu, Q. Yao, C. Wu, Calcium silicate nanowires-containing multicellular bioinks for 3D bioprinting of neural-bone constructs, Nano Today 46 (2022) 101584.

[15] H. Zhang, H. Huang, G. Hao, Y. Zhang, H. Ding, Z. Fan, L. Sun, 3D printing hydrogel scaffolds with nanohydroxyapatite gradient to effectively repair osteochondral defects in rats, Adv. Funct. Mater. 31 (1) (2021) 2006697.

[16] Q. Yu, Y. Han, X. Wang, C. Qin, D. Zhai, Z. Yi, J. Chang, Y. Xiao, C. Wu, Copper silicate hollow microspheres-incorporated scaffolds for chemo-photothermal therapy of melanoma and tissue healing, ACS Nano 12 (3) (2018) 2695–2707.

[17] Z. Wan, Z. Yuan, Y. Li, Y. Zhang, Y. Wang, Y. Yu, J. Mao, Q. Cai, X. Yang, Hierarchical therapeutic ion-based microspheres with precise ratio-controlled delivery as microscaffolds for in situ vascularized bone regeneration, Adv. Funct. Mater. 32 (23) (2022) 2113280.

[18] S. Wu, C. Mou, H. Lin, Synthesis of mesoporous silica nanoparticles, Chem. Soc. Rev. 42 (9) (2013) 3862–3875.

[19] J.G. Croissant, K.S. Butler, J.I. Zink, C.J. Brinker, Synthetic amorphous silica nanoparticles: toxicity, biomedical and environmental implications, Nat. Rev. Mater. 5 (12) (2020) 886–909.

[20] F. Jiang, L. Zhang, Z. Jiang, C. Li, D. Cang, X. Liu, Y. Xuan, Y. Ding, Diatomite-based porous ceramics with high apparent porosity: pore structure modification using calcium carbonate, Ceram. Int. 45 (5) (2019) 6085–6092.

[21] Z. Jia, T. Li, Z. Zheng, J. Zhang, J. Liu, R. Li, Y. Wang, X. Zhang, Y. Wang, C. Fan, The BiOCl/diatomite composites for rapid photocatalytic degradation of ciprofloxacin: efficiency, toxicity evaluation, mechanisms and pathways, Chem. Eng. J. 380 (2020) 122422.

[22] C. Feng, J. Li, G.S. Wu, Y.Z. Mu, M. Kong, C.Q. Jiang, X.J. Cheng, Y. Liu, X.G. Chen, Chitosan-coated diatom silica as hemostatic agent for hemorrhage control, ACS Appl. Mater. Interfaces 8 (50) (2016) 34234–34243.

[23] S. Maher, M. Alsawat, T. Kumeria, D. Fathalla, G. Fetih, A. Santos, F. Habib, D. Losic, Luminescent silicon diatom replicas: self-reporting and degradable drug carriers with biologically derived shape for sustained delivery of therapeutics, Adv. Funct. Mater. 25 (32) (2015) 5107–5116.

[24] J. Ma, J. Wu, H. Zhang, L. Du, H. Zhuang, Z. Zhang, B. Ma, J. Chang, C. Wu, 3D printing of diatomite incorporated composite scaffolds for skin repair of deep burn wounds, Int. J. Bioprinting 8 (3) (2022) 163–175.

[25] Y. Wang, Z. Yuan, Y. Pang, T. Wang, X. Wang, G. Li, X. Zhang, Y. Yu, X. Yang, Q. Cai, Injectable, high specific surface area cryogel microscaffolds integrated with osteoinductive bioceramic fibers for enhanced bone regeneration, ACS Appl. Mater. Interfaces 15 (17) (2023) 20661–20676.

[26] L. Zhang, Y. Pang, Y. Tang, X. Wang, D. Zhang, X. Zhang, Y. Yu, X. Yang, Q. Cai, Multileveled hierarchical hydrogel with continuous biophysical and biochemical gradients for enhanced repair of full-thickness osteochondral defect, Adv. Mater. 35 (19) (2023) 2209565.

[27] L. Wang, Y. Pang, Y. Tang, X. Wang, D. Zhang, X. Zhang, Y. Yu, X. Yang, Q. Cai, A biomimetic piezoelectric scaffold with sustained Mg²⁺ release promotes neurogenic and angiogenic differentiation for enhanced bone regeneration, Bioact. Mater. 25 (2023) 399–414.

[28] X. Wang, W. Dai, C. Gao, L. Zhang, Z. Wan, T. Zhang, Y. Wang, Y. Tang, Y. Yu, X. Yang, Q. Cai, Spatiotemporal modulated scaffold for endogenous bone regeneration via harnessing sequentially released guiding signals, ACS Appl. Mater. Interfaces 15 (50) (2023) 58873–58887.

[29] L. Fu, L. Li, Q. Bian, X. Bue, J. Jin, J. Li, Y. Cao, Q. Jiang, H. Li, Cartilage-like protein hydrogels engineered via entanglement, Nature 618 (7966) (2023) 740–747.

[30] S. Choi, J.R. Moon, N. Park, J. Im, Y.E. Kim, J.-H. Kim, J. Kim, Bone-adhesive anisotropic tough hydrogel mimicking tendon enthesis, Adv. Mater. 35 (3) (2023) 2206207.

[31] C. Gao, W. Dai, X. Wang, L. Zhang, Y. Wang, Y. Huang, Z. Yuan, X. Zhang, Y. Yu, X. Yang, Q. Cai, Magnesium gradient-based hierarchical scaffold for dual-lineage regeneration of osteochondral defect, Adv. Funct. Mater. 33 (43) (2023) 2304829.

[32] G. Chen, X. Liang, P. Zhang, S. Lin, C. Cai, Z. Yu, J. Liu, Bioinspired 3D printing of functional materials by harnessing enzyme-induced biomineralization, Adv. Funct. Mater. 32 (34) (2022) 2113262.

[33] W. Qiao, K.H.M. Wong, J. Shen, W. Wang, J. Wu, J. Li, Z. Lin, Z. Chen, J. P. Matinlinna, Y. Zheng, S. Wu, X. Liu, K.P. Lai, Z. Chen, Y.W. Lam, K.M.C. Cheung, K.W.K. Yeung, TRPM7 kinase-mediated immunomodulation in macrophage plays a central role in magnesium ion-induced bone regeneration, Nat. Commun. 12 (1) (2021) 2885.

[34] R. Yang, G. Li, C. Zhuang, P. Yu, T. Ye, Y. Zhang, P. Shang, J. Huang, M. Cai, L. Wang, W. Cui, L. Deng, Gradient bimetallic ion-based hydrogels for tissue microstructure reconstruction of tendon-to-bone insertion, Sci. Adv. 7 (26) (2021) eabg3816.

[35] C. Qin, J. Ma, L. Chen, H. Ma, H. Zhuang, M. Zhang, Z. Huan, J. Chang, N. Ma, C. Wu, 3D bioprinting of multicellular scaffolds for osteochondral regeneration, Mater. Today 49 (2021) 68–84.

[36] O. Chaudhuri, J. Cooper-White, P.A. Janmey, D.J. Mooney, V.B. Shenoy, Effects of extracellular matrix viscoelasticity on cellular behaviour, Nature 584 (7822) (2020) 535–546.

[37] Z. Ma, C. Bourquard, Q. Gao, S. Jiang, T. De Iure-Grimmel, R. Huo, X. Li, Z. He, Z. Yang, G. Yang, Y. Wang, E. Lam, Z. Gao, O. Supponen, J. Li, Controlled tough bioadhesion mediated by ultrasound, Science 377 (6607) (2022) 751–755.

[38] L. Yu, Y. Hou, W. Xie, J.L. Cuellar-Camacho, Q. Wei, R. Haag, Self-strengthening adhesive force promotes cell mechanotransduction, Adv. Mater. 32 (52) (2020) 2006986.

[39] F.J. Vernerey, S.L. Sridhar, A. Muralidharan, S.J. Bryant, Mechanics of 3D cell-hydrogel interactions: experiments, models, and mechanisms, Chem. Rev. 121 (18) (2021) 11085–11148.

[40] D. Huang, Y. Li, Z. Ma, H. Lin, X. Zhu, Y. Xiao, X. Zhang, Collagen hydrogel viscoelasticity regulates MSC chondrogenesis in a ROCK-dependent manner, Sci. Adv. 9 (6) (2023) eade949.

[41] C. Zhou, M. Duan, D. Guo, X. Du, D. Zhang, J. Xie, Microenvironmental stiffness mediates cytoskeleton re-organization in chondrocytes through laminin-FAK mechanotransduction, Int. J. Oral Sci. 14 (1) (2022) 15.

[42] R. Sheng, J. Liu, W. Zhang, Y. Luo, Z. Chen, J. Chi, Q. Mo, M. Wang, Y. Sun, C. Liu, Y. Zhang, Y. Zhu, B. Kuang, C. Yan, H. Liu, L.J. Backman, J. Chen, Material stiffness in cooperation with macrophage paracrine signals determines the tenogenic differentiation of mesenchymal stem cells, Adv. Sci. 10 (17) (2023) 2206814.

[43] M.C. Arno, M. Inam, A.C. Weems, Z. Li, A.L.A. Binch, C.I. Platt, S.M. Richardson, J. A. Hoyland, A.P. Dove, R.K. O'Reilly, Exploiting the role of nanoparticle shape in enhancing hydrogel adhesive and mechanical properties, Nat. Commun. 11 (1) (2020) 1420.

[44] C. Deng, Q. Yang, X. Sun, L. Chen, C. Feng, J. Chang, C. Wu, Bioactive scaffolds with Li and Si ions-synergistic effects for osteochondral defects regeneration, Appl. Mater. Today 10 (2018) 203–216.

[45] L. Chen, C. Deng, J. Li, Q. Yao, J. Chang, L. Wang, C. Wu, 3D printing of a lithium-calcium-silicate crystal bioscaffold with dual bioactivities for osteochondral interface reconstruction, Biomaterials 196 (2019) 138–150.

[46] P. Bhattacharjee, B. Kundu, D. Naskar, H.-W. Kim, T.K. Maiti, D. Bhattacharya, S. C. Kundu, Silk scaffolds in bone tissue engineering: an overview, Acta Biomater. 63 (2017) 1–17.

[47] V. Bunpetch, X. Zhang, T. Li, J. Lin, E.P. Maswikiti, Y. Wu, D. Cai, J. Li, S. Zhang, C. Wu, H. Ouyang, Silicate-based bioceramic scaffolds for dual-lineage regeneration of osteochondral defect, Biomaterials 192 (2019) 323–333.

[48] M. Shi, Y. Zhou, J. Shao, Z. Chen, B. Song, J. Chang, C. Wu, Y. Xiao, Stimulation of osteogenesis and angiogenesis of hBMSCs by delivering Si ions and functional drug from mesoporous silica nanospheres, Acta Biomater. 21 (2015) 178–189.

[49] R. Li, Z. Zhu, B. Zhang, T. Jiang, C. Zhu, P. Mei, Y. Jin, R. Wang, Y. Li, W. Guo, C. Liu, L. Xia, B. Fang, Manganese enhances the osteogenic effect of silicon-hydroxyapatite nanowires by targeting T lymphocyte polarization, Adv. Sci. (2023) 2305890.

[50] S. Zhang, Y. Cui, X. Ma, J. Yong, L. Yan, M. Yang, J. Ren, F. Tang, L. Wen, J. Qiao, Single-cell transcriptomics identifies divergent developmental lineage trajectories during human pituitary development, Nat. Commun. 11 (1) (2020) 5275.

[51] Q. Li, H. Yu, M. Sun, P. Yang, X. Hu, Y. Ao, J. Cheng, The tissue origin effect of extracellular vesicles on cartilage and bone regeneration, Acta Biomater. 125 (2021) 253–266.

[52] A.K. Huber, N. Patel, C.A. Pagani, S. Marini, K.R. Padmanabhan, D.L. Matera, M. Said, C. Hwang, G.C. Hsu, A.A. Poli, A.L. Strong, N.D. Visser, J.A. Greenstein, R. Nelson, S. Li, M.T. Longaker, Y. Tang, S.J. Weiss, B.M. Baker, A.W. James, B. Levi, Immobilization after injury alters extracellular matrix and stem cell fate, J. Clin. Invest. 130 (10) (2020) 5444–5460.

[53] Z. Cai, Y. Tang, Y. Wei, P. Wang, H. Zhang, Double - network hydrogel based on exopolysaccharides as a biomimetic extracellular matrix to augment articular cartilage regeneration, Acta Biomater. 152 (2022) 124–143.